Title
Developing droplet microfluidic technologies for single-cell and single-molecule assays

Author
Kahkeshani, Soroush

Publication Date
2017

Peer reviewed|Thesis/dissertation

UNIVERSITY OF CALIFORNIA

Los Angeles

Developing droplet microfluidic technologies for single-cell and single-molecule assays

A dissertation submitted in partial satisfaction of the

requirements for the degree Doctor of Philosophy

in Bioengineering

by

Soroush Kahkeshani

2017

ABSTRACT OF THE DISSERTATION

Developing droplet microfluidic technologies for single-cell and single-molecule assays

by

Soroush Kahkeshani

Doctor of Philosophy in Bioengineering

University of California, Los Angeles, 2017

Professor Dino Di Carlo, Chair

In the past decade, growing number of commercialized “lab on a chip” systems have been addressing needs in biology for patients and researchers. The ability to miniaturize conventional systems used in lab while increasing sensitivity in addition to newly developed platforms, have enabled new applications such as point-of-care diagnostics and single-cell sequencing. This dissertation focuses on new droplet microfluidic platforms developed for addressing the current challenges (controlling encapsulation beyond Poisson distribution, removing bulky and expensive pumps,…) in commercialization of single-cell and single-molecule assays. In chapter 1, current state of the art, recent commercialized products and their limitations are discussed.

In chapter 2, new findings about particle interactions in single-phase microfluidics leading to “preferred interparticle spacings” and trajectory attractors in inertial microflow regimes are

presented. Furthermore, these findings have been combined with new modifications made to conventional flow focusing droplet generators in order to avoid jetting regime in inertial regimes, thus allowing making use of preferred spacing between cells/particles in inertial flows for controlling number of cells/particles encapsulated in droplets (one cell/particle per drop). Our findings could be used for many applications such as drug discovery. The other application could be for droplet sequencing (drop-seq) where for example RNA of individual cells are sequenced and it is important that only one cell is present in each droplet to generate unbiased data.

In chapter 3 and 4 of the dissertation, new patented technology for generation of droplets, replacing bulky and expensive pumps, with body force exerted on the ferrofluid by magnetic field acting on magnetic nanoparticles mixed with the fluid. Thus the cost and footprint of the device is reduced significantly, allowing for use in limited-resource settings (global health) for quantification of biomolecules by controlled magnetic dosing of nanoliter droplets.

This dissertation of Soroush Kahkeshani is approved.

Jeffrey Eldredge

Pei-Yu Chiou

Marcus Roper

Dino Di Carlo, Committee Chair

University of California, Los Angeles

2017

DEDICATION

Humbly dedicated to:

Mitra, Mehdi, Soheil, all my friends and mentors

TABLE OF CONTENTS

ACKNOWLEDGEMENTS

Chapter 1

Commercialized droplet microfluidic technologies for single cell and single molecule applications is an introductory chapter by S. Kahkeshani and D. Di Carlo. The chapter focuses on recent commercialized products in the last 5 years involving droplet technologies. Limitations and potential improvements that could be done based on the findings discussed in the next chapters of the dissertation are discussed.

Chapter 2

Inertial single-phase microfluidic flows integrated with multiphase microfluidic systems for single cell applications has been reprinted with minor adaptations with permission from (Kahkeshani S, Haddadi, H and Di Carlo D **Journal of fluid mechanics, 2016, 786, R3** *Preferred interparticle spacings in trains of particles in inertial microchannel flows*), with addition of the new results that are in preparation for another publication (journal paper) regarding integration with multiphase microfluidic systems for single cell applications. Professor Dino Di Carlo is the principal investigator of this work. This project received funds from ONR. Lattice Boltzmann simulations are done by Dr. Hamed Haddadi.

Chapter 3

Drop formation using ferrofluids driven magnetically in a step emulsification device has been reprinted with minor adaptations with permission from (Kahkeshani S and Di Carlo D 2016 **Lab on a chip**). Professor Dino Di Carlo is the principal investigator of this work. This project

received funds from National Science of Foundation grant no. 1332275.

Chapter 4

Magnetic nanoliter drop dosing device for point of care quantification of DNA is a version of work in progress for publication by S. Kahkeshani, J. Kong, D. Tseng, Q. Wei, O. Garner, Aydogan. Ozcan, Dino Di Carlo.

Professor Dino Di Carlo is the principal investigator of this work. This project received funds from National Science of Foundation. The imaging system is developed by Ozcan lab at UCLA.

VITA

Education

B.Sc. in Mechanical Engineering 2009-2013

Sharif University of Technology, Tehran, Iran

Project: Pinch flow fractionation of cancer cells from blood in microchannels

Awards and Honors

• Recipient of the Bioengineering department fellowship for graduate studies, UCLA, 2013-2015

• Recipient of the grant for undergraduate studies from the Iranian National Elites Foundation, for outstanding academic success, 2009-2013.

• Bronze Medalist in National Physics Olympiad. Iran, 2008

•Member of the National Organization for Development of Exceptional Talents, Iran. 2005-present

Publications

Journal Papers:

• S. Kahkeshani, J. Kong, Q. Wei, D. Tseng, O. Garner, A. Ozcan and D. Di Carlo, Magnetic nanoliter droplet dosing device for point of care quantification of DNA molecules, In preparation 2017.

• S. Kahkeshani and D. Di Carlo, Drop formation using ferrofluids driven magnetically in a step emulsification device, Lab Chip, 2016, 16, 2474-2480

• S. Kahkeshani, H. Haddadi, and D. Di Carlo, Preferred interparticle spacings in trains of

particles in inertial microchannel flows, J. Fluid Mech., 2016, 786, R3.

•K. Hood, S. Kahkeshani, D. Di Carlo and M. Roper, Direct measurement of particle inertial migration in rectangular microchannels, Lab Chip. 2016, 16 (15), 2840-2850

Patent

S. Kahkeshani and D. Di Carlo, Systems and methods for droplet formation and manipulation using ferrofluids, **PCT/US16/56148**. (for point-of-care diagnostics and also implantable/wearable drug delivery) –filed 2015

Conferences

• J. Kong, S.Kahkeshani, J. Hambalek, M. Margolis, and D. Di Carlo, Magnitude improvement in signal applied to digital nucleic acid amplification tests

EMBS micro and nanotechnology in medicine conference, 2016

• S. Kahkeshani and D. Di Carlo, Different modes of self-assembly in inertial micro channel flows.

American physical society meeting, Division of fluid dynamics, 2014.

• K. Hood, S. Kahkeshani, D. Di Carlo and M. Roper. Tuning particle focusing in inertial microfluidics.

American physical society meeting, Division of fluid dynamics, 2015

Chapter 1

Recent commercialized droplet microfluidic platforms for single-cell and single-molecule assays- Limitations and Future

Abstract:

In recent years there has been extensive effort to commercialize micro technologies for single cell and single molecule applications. However, there are not many commercialized technologies available related to droplet microfluidics due to: (1) dependence of the droplet generation systems on bulky, sensitive and expensive pumps (2) Sensitivity of the droplet formation regime (dripping, tip streaming, …) on flow rates (3) need for accurate imaging systems for detection of individual micron sized droplets while controlling their movements. Here in this introductory chapter we focus on the recent commercialized droplet microfluidic (DMF) products in the last 5 years for single cell and single molecule assays using droplet microfluidics. In addition we also discuss their limitations and how my work during my PhD (categorized in the next 3 chapters) have addressed some of these challenges by:

(1) Modifying flow focusing droplet generator so that relatively high flow rates could be achieved in the inertial regime without jetting and using preferred interparticle spacing for controlling number of particles/cells encapsulate in droplets –avoiding two cell per droplet for single cell assays- discussed in **chapter 2.**

(2) Developing a new droplet generation technique driven using a small magnet using ferrofluids, thus removing the need for bulky and expensive pumps for limited resource and point of care settings- discussed in **chapter 3.**

(3) Developing new method and device for quantification of biomolecules in multiplexed assays using our magnet droplet generator using a simple cell-phone imaging system removing the need for imaging individual micron sized droplets- discussed in **chapter 4.**

Introduction

Why Droplet microfluidics?

Droplet microfluidics provides a tool for isolating biological entities from a population, thus makes studying single cells possible. It also enables partitioning of the sample containing target molecules and number of droplets containing the molecules, revealed by the fluorescent signal or other techniques could be used for quantification of molecules. Droplet microfluidic systems are commonly used and can easily be integrated with different fluidic designs unlike nano-well compartmentalization and valving methods.

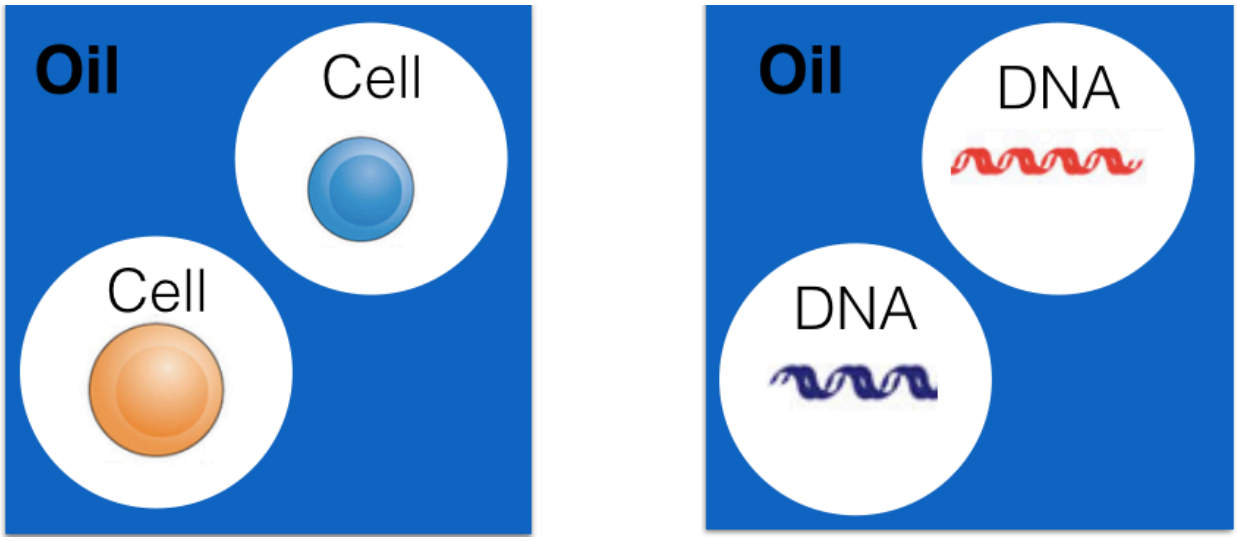

Figure 1: Droplets enable isolation of cells and molecules in controlled conditions for different applications.

Why single cell studies?

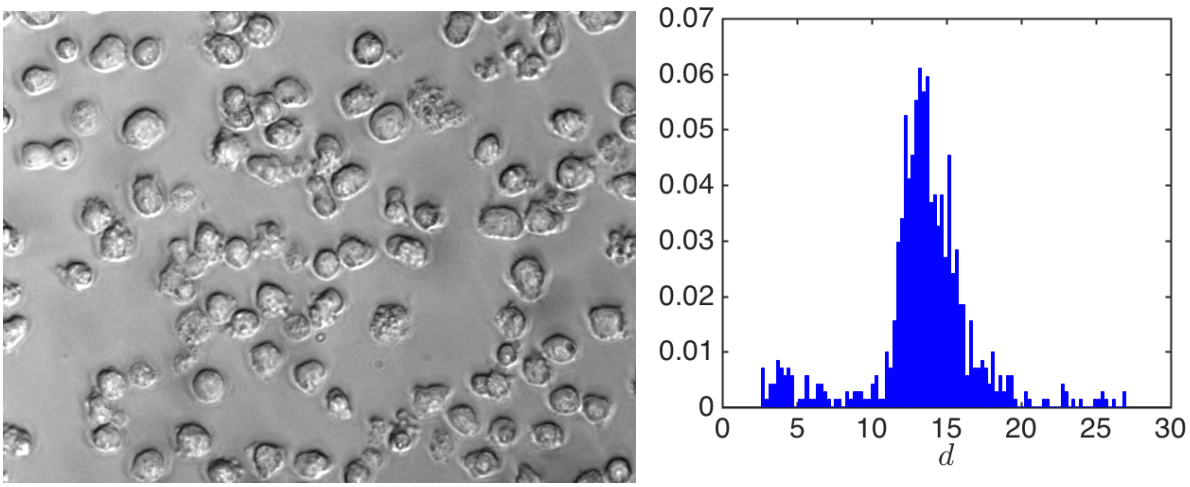

Figure 2: HL 60 cells and size distribution (diameter of cells in micron).

Single cell studies are crucial for a range of applications. In a population of cells, there is cell to cell heterogeneity as shown in figure 1, and each cell could show a different response to a drug, and in fact the heterogeneity in the population could reveal valuable findings for example regarding cancer prognosis. Other areas showing importance of single cell studies is related to differentiation of stem cells, sequencing of single cells and drug discovery.

Why single molecule detection?

Another area, which is benefiting from droplet microfluidic platforms, is digital (droplet) diagnostics for single molecule detection. The number of target molecules in a sample could reveal important information about patient's health. Steps that need to be taken in serious cases are different from low risk conditions, thus only a yes/no answer for presence of a molecule is

not valuable and precise quantification of molecules is needed. Droplets allow compartmentalization of sample to nano and pico liter volumes. Therefore, instead of running assays on the whole solution at once, parallel experiments in each droplet can be performed and droplets containing target molecules will result in amplified signal, change of color or other changes that reveals presence of a target molecule. Based on the number of droplets that show the change, concentration of DNA in the original sample could be determined.

Here we discuss recent commercialized products for cell line development, genomics, digital (droplet) diagnostics and how recent findings discussed in the next chapters of the dissertation could potentially improve these systems:

Cytena:

Although droplets enable us to encapsulate cells and isolate them, controlling number of encapsulated particle/cells per droplets is not an easy task. Researchers have addressed this problem from both fluid mechanics and technological standpoints. Cytena is using an advanced imaging system for this purpose.

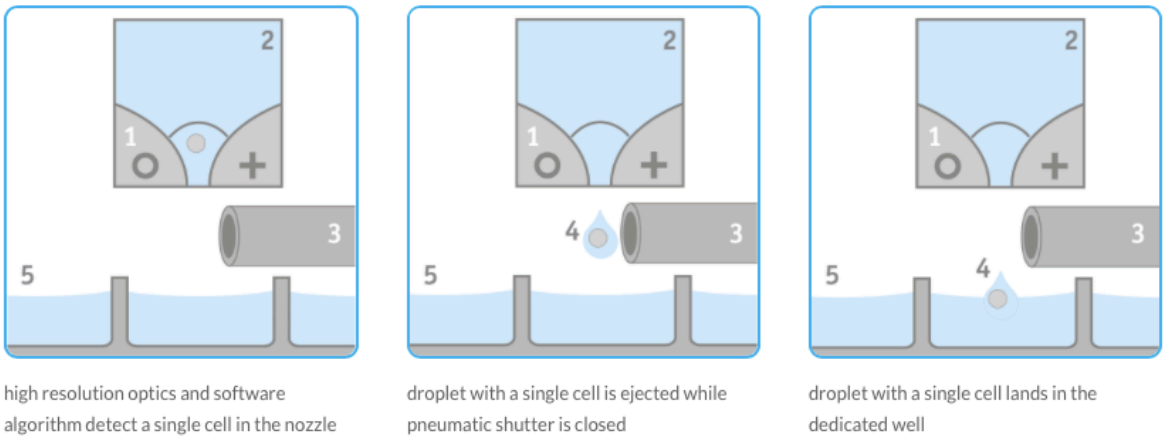

Figure 3: Process of detecting and ejecting single-cells into wells using high-resolution optics (reprinted from Cytena website with permission).

The single-cell printing technology, enables fully automated isolation of single cells into standard microwell plate formats. The instrument uses an inkjet-like principle featuring a disposable, one-way printing cartridge.

The cell sample is pipetted into the cartridge and an external actuator is used to eject droplets out of it. The integrated optical sensor allows for determination of cell number in each droplet. A fast shutter mechanism sorts the droplets containing exactly one single-cell into the substrate. Unwanted droplets are deflected into waste. The disposable cartridge takes 80 µl of cell sample. Then silicon microfluidic chip generates pico liter droplets.

Limitations and potential solutions:

The system could be improved in 2 different aspects: 1) controlling particle frequencies beyond poisson distribution. 2) Using passive force generation system to avoid the time required for processing and actuation allowing development of high-throughput systems.

Wafergen biosystems - Icell 8 system multi sample nano dispenser:

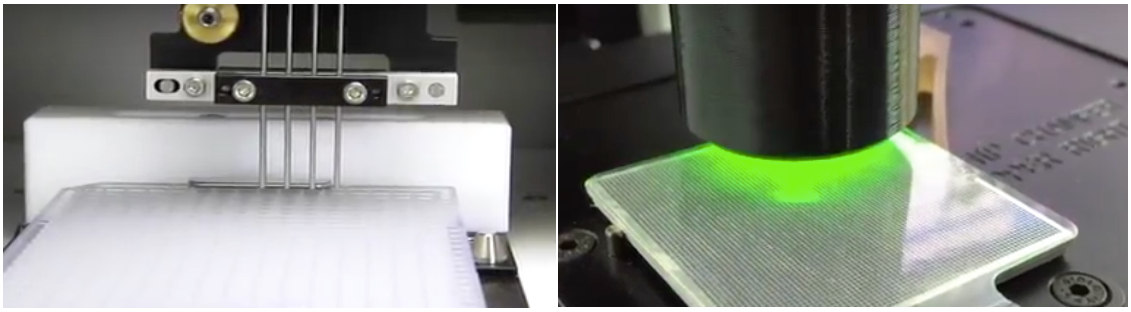

Figure 4: Nano dispensing of the sample in each well and then detecting the wells that contain only one cell using imaging system and continue the experiments with those wells (reprinted from Wafergen biosystems website with permission).

The MultiSample NanoDispenser (MSND) deposits nanoliter volumes of cells and reagents into the ICELL8 Chip in a temperature and humidity controlled environment. The MSND is capable of dispensing 8 unique samples evenly across the chip in 15 minutes. The rapid dispensing and environmental control helps to ensure sustained cell viability throughout the cell isolation process. Then the imaging system identifies the wells that contain only one cell and uses those wells for the rest of the process. This method is also similar to the one that Cytena company uses, however here instead of detecting the droplet that contain only once cell and then releasing them, all the wells are filled by nano dispensing and later the wells containing one cell will be identified by imaging. Same limitations and possible improvemens could be applied to this platform as we discussed for the previous product by Cytena company.

10x genomics:

As they report in nature biotechnology paper (2016), barcoded gel beads are used, and they are mixed with DNA solution and then emulsified in flow focusing droplet generator made of plastic. Up to 8 samples could be processed simultaneously. Since a concentrated pack of gel beads is used for this purpose, more than 85% of droplets contain only 1 bead. Gels are dissolved and primers are released due to presence of a chemical in the reaction mixture and then thermo cycling is done. Finally the purified solution is used for sequencing for Haplotyping germline and cancer genomes studies. For DNA applications, they start with only 1 ng of DNA. For single-cell applications, they start with thousands of cells to achieve optimum results.

Limitations and potential solutions:

In this platform the higher efficiency of trapping only one bead/cell in each droplet, the higher the accuracy of the results will be. To achieve that, 10x genomics uses concentrated solution of gel beads to ensure having one bead per droplet. However this might lead to clogging of the channel or increasing the possibility of having more than one bead per droplet. One way to address this problem is by understanding how particles/cell form trains in inertial flows in microchannels. That is, at slightly high flow rates where it's still possible to generate droplets (avoid jetting), investigate how interparticle spacing changes in a suspension. As I have studied this problem in my PhD, and we have published the results in Journal of fluid mechanics in 2016, there are preferred interparticle spacings depending on the particle Reynolds (see chapter 2 of the dissertation). For example at low flow rates the preferred spacing is around 5D, where D is

the particle diameter. Therefore, by adjusting oil flow rate and droplet generation frequency, number of encapsulated partciles/cells per droplet is controlled (1 per drop or 2 per drop).

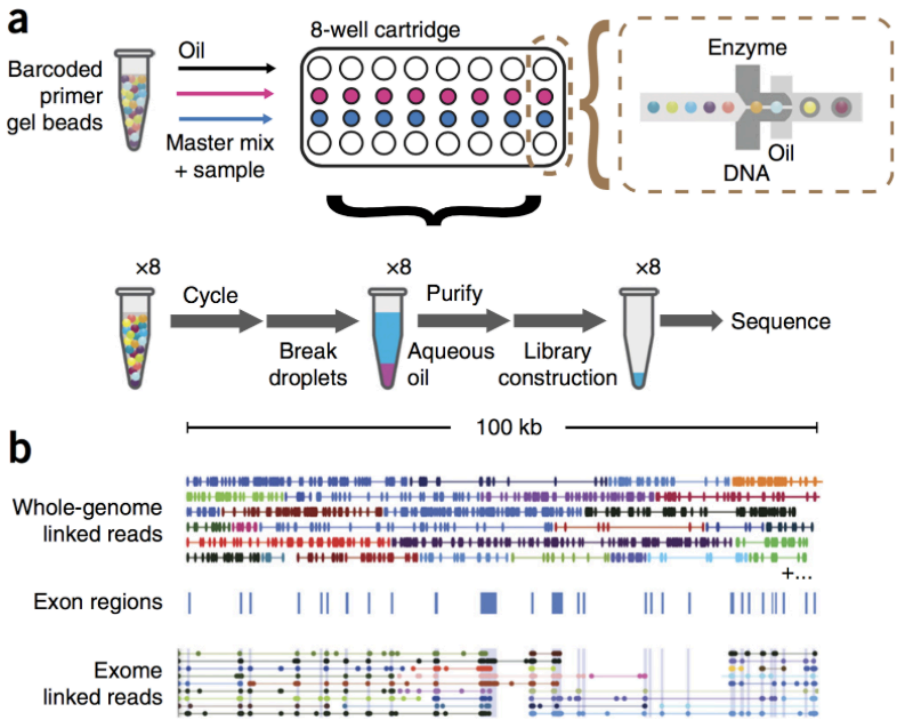

Figure 5: Working process of sequencing using 10x genomics platform with barcoded primer gel beads and DNA sample (reprinted from nature biotechnology 2016 with permission).

Biorad-Illumina ddSEQ™ Single-Cell Isolator:

The ddSEQ Single-Cell Isolator is part of the Illumina® Bio-Rad® Single-Cell Sequencing Solution. This technology utilizes disposable microfluidic cartridges to coencapsulate single cells and barcodes into subnanoliter droplets, where cell lysis and barcoding occur. RNA-Seq libraries are subsequently prepared and sequenced. Analysis is conducted via BaseSpace.

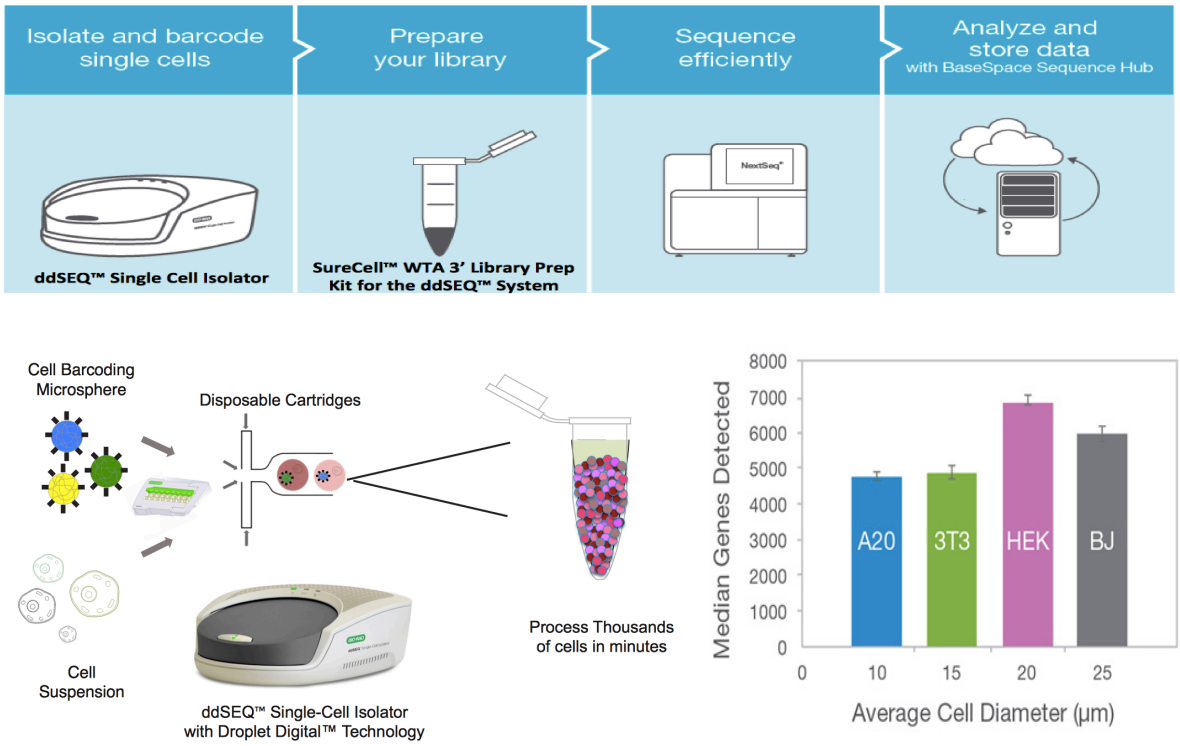

Figure 6: ddseq uses a flow focusing droplet generator for co-encapsulating single cells and barcoding micro particles and it can process thousands of cells in minutes (reprinted from Biorad website with permission).

Limitations and potential solutions:

Here also similar to the products by Cytena and 10x genomics and wafergen biosystems, controlling spacing between particles/cells before droplet formation could significantly increase single cell encapsulation efficiency (see chapter 2 of the dissertation).

Eplex system-Genmark (with liquid logic)

Fully integrates nucleic acid extraction, amplification, and detection

Sample to result in 60-90 minutes. Versatile fluid management is done using digital microfluidics and electro-wetting. Electrochemical detection technology is used and multiplexing can be achieved using this platform.

Figure 7: Sample is poured in the cartridge and then it is inserted into device for processing

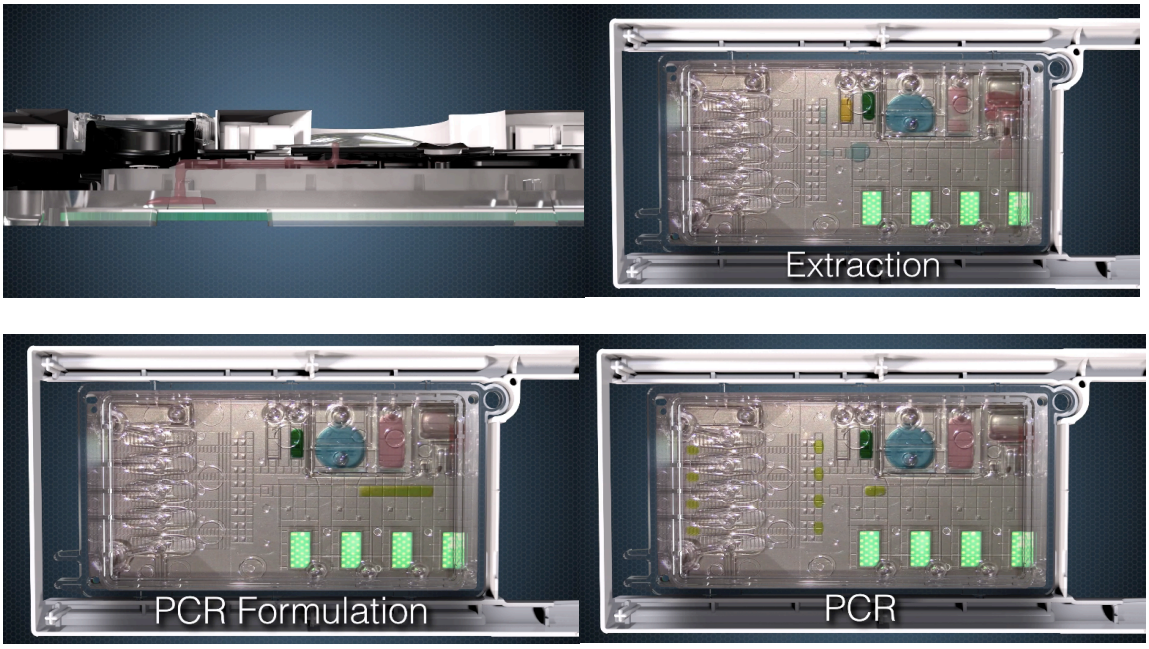

Figure 8: Detailed view of the process that happens once the cartridge is inserted into the device. Using electro-wetting, nano liters of sample could be manipulated precisely for PCR (reprinted from Genmark website with permission).

Limitations and potential solutions:

This platform is bulky and requires operation in the lab, thus limiting its application for point-of-care and limited-resource settings. Droplet generation and manipulation system that does not depend on complex and expensive equipment could expand application of droplet diagnostic systems. (see chapter 3 and 4 of the dissertation)

QX200™ Droplet Digital™ PCR System:

The QX200 Droplet Digital PCR system provides absolute quantification of target DNA or RNA molecules for EvaGreen or probe-based digital PCR applications. Droplet partitioning by the QX200 Droplet Digital technology (nanoliters) reduces bias from amplification efficiency and PCR inhibitors. The PCR-positive and PCR-negative droplets are counted to provide absolute quantification of target DNA in digital form.

Figure 9: Workflow and components of the ddPCR system (reprinted from Biorad website with permission).

Limitations and potential solutions:

This product is similar to Biorad-Illumina ddSEQ™ Single-Cell Isolator that is discussed earlier. The difference is in the application which requires thermocycling in PCR and a separate device is used for imaging which could not be used for point-of-care in a limited resource settings.

Conclusion

Although droplet microfluidic platforms have been used for almost two decades, but still number of commercialized products using these systems is limited due to limitations and complexities associated with them such as bulky and expensive pumps, and sensitivity to flow rates leading to jetting regime at higher flow rates. In the next chapters these issues have been addressed for

single-cell and single-molecule applications.

Chapter 2

Inertial single-phase microfluidic flows integrated with multiphase microfluidic systems for single cell applications

Abstract

Suspended particles migrate toward inertial focusing positions close to walls and align into trains in finite inertia conduit flow. The relative contribution of inertial to viscous forces at the particle length scale, defined by the particle Reynolds number Re_p is a key parameter, where $Re_p = \gamma \cdot D^2/v$ depends on the mean shear rate $\gamma \cdot$, particle diameter D and fluid kinematic viscosity v. Controlling the location of inertial focusing positions and the interparticle distance is critical in applications such as flow cytometry, imaging and cell entrapment in droplets. By using experimental observations in rectangular microchannels and lattice-Boltzmann numerical simulations of dilute suspension flow, the spacing between particles aligned in trains is measured. From the modes of the probability density function of interparticle spacing, preferred spacings at *5D* and *2.5D* are observed. At lower Re_p, the preferred spacing forms around *5D* and with increasing Re_p the spacing at *2.5D* becomes more pronounced. With increasing concentration of the suspension the spacing is influenced by particle crowding effects until stable trains are no longer observed.

Introduction

Migration of particles towards inertial focusing positions and formation of particle trains are prominent examples of inertial effects in flow of dilute suspensions in conduits (Segre & Silberberg 1961; Matas et al. 2004). Using a characteristic velocity U, length scale L and fluid kinematic viscosity υ, flow inertia is characterized by Reynolds number defined as $Re = \frac{UL}{\upsilon}$. In confined geometries, such as microchannels, the inertial flow of dilute suspensions has been utilized to self-assemble particles into trains at inertial focusing positions (Di Carlo et al. 2007; Di Carlo et al. 2009; Hur, Tse & Di Carlo 2010; Lee et al. 2010). Although the number of trains and the location of focusing positions can be engineered by changing channel dimensions and flow inertia (Chun & Ladd 2006; Amini, Lee & Di Carlo 2014), controlling the interparticle spacing necessitates understanding hydrodynamic interaction between particles. Controlling the distance between particles is crucial for applications such as high speed imaging, flow cytometry and entrapment of live cells in droplets for tissue printing applications, where knowing the arrival time of particles aids in adjusting the imaging or cell entrapment sequence. (Edd et al. 2008).

The inertial ordering of particles in trains and interparticle spacings have been experimentally observed in tubular conduits and rectangular microchannels (Matas et al. 2004; Hur, Tse & Di Carlo 2010). While the underlying mechanism for inertial migration of particles towards focusing positions can be explained by analytical solution of the lateral force on isolated particles (Ho & Leal 1976; Asmolov 1999; Hood, Lee & Roper 2015), the quantitative and predictive models for the spacing between particles self-assembled in trains is more difficult to ascertain

due to complexity of hydrodynamic interactions between multiple moving particles at finite *Re* (Martel & Toner 2014). By studying inertial flow of a dilute suspension in tubes of *O(10 mm)* diameter, the underlying mechanism for train formation was attributed to the presence of reversing streamline regions, where fluid parcels approach the particle surface and reverse their paths (Matas et al. 2004). Numerical studies of hard sphere suspensions at dilute to intermediate concentrations under finite inertia shear flow show that the reversing motion also exists in relative trajectories of particles with respect to one another (Haddadi & Morris 2014; Haddadi & Morris 2015). By increasing *Re*, the size of the reversing flow region increases which leads to a closer distance between particles and a monotonic reduction of the average interparticle spacing in trains (Matas et al. 2004). Through experimental study of the reversing streamlines in microchannels, it has been demonstrated that due to an interplay between viscous disturbance flow, which deviates the particles from inertial focusing points and inertial lift force which tends to restore particle location, the average spacing between particles changes until reaching an equilibrium value in the channel downstream (Lee et al. 2010). Although explained in a phenomenological manner, there remains no general predictive model for interparticle spacing. The lateral and axial ordering of particles in microchannels have been studied by changing the concentration of the suspension and dimensions of the channel cross section. Increasing the concentration of the suspension leads to formation of multiple trains for certain channel dimensions. A preferred interparticle spacing also forms around *2.2D* (Humphry et al. 2010).

In the present work, experiments and numerical simulations have been employed to study the effect of inertia and concentration on the spacing between particles dynamically self-assembled into trains in microchannels. The axial distance between two consecutive particles, denoted as

d_x, depends on the conduit Reynolds number Re_c which is defined using hydraulic diameter as the characteristic length scale. Inertia can also be defined at the particle length scale by Re_p, determined by the shear rate and diameter of the particle. For a pressure driven flow in a channel with rectangular cross section (channel schematic displayed in figure 1), a parabolic velocity profile along with the difference between channel dimensions in *Y* and *Z* directions leads to a varying shear rate on the particle. For a channel with aspect ratio of *0.58*, which is defined as $\lambda = \frac{l_y}{l_z}$, particles are expected to equilibrate near the longer walls in *Y* direction (Amini, Lee & Di Carlo 2014). Therefore, Re_p can be defined using the mean shear rate, particle diameter *D* and the channel length in the *Y* direction (l_y) as $Re_p = (\frac{D}{l_y})^2 Re_y$, where $Re_y = <u>\frac{l_y}{\upsilon}$. Matas et al. (2004) examined the spacing between particles within trains in *O(10 mm)* tube flow and reported a monotonic reduction of the *average* interparticle spacing. Here, the discussion is focused on the most probable spacing between consecutive particles in trains inside a rectangular microchannel, which is important for microchannel imaging and cell sorting applications. In order to measure the location of the most probable spacing, the probability density function of the interparticle distance has been computed for particles self-assembled into trains and the modes, which distinctly form in curves of the probability density function are chosen as a metric of the *preferred* spacing. The effect of Re_p on the axial spacing between consecutive particles (d_x) has been studied for suspensions of $\emptyset \sim$ *O (0.001)* concentration. It will be shown that the preferred spacing between particles switches from *5D* for low Re_p to *2.5D* at higher Re_p, without the presence of intermediate values. The results also demonstrate that increasing the concentration of suspensions to *O (0.01)* results in the reduction of the distance between particles in trains and the preferred spacings measured for $\emptyset \sim$*O (0.001)* suspensions will no longer form. Further increase

of $\emptyset$ leads to unsteadiness in the spacing and prevents self-assembly of particles into ordered trains.

Experimental procedure

The experimental observations have been made in a dual inlet polydimethylsiloxane microchannel bonded to a glass slide produced according to standard soft lithography protocols (Duffy et al. 1998). The dual inlet channel is utilized in order to self-assemble particles predominantly into one train in order to limit hydrodynamic interactions between particles to a single train. Dimensions of the channel in the axial (*X* or flow direction), lateral (*Y*) and transverse (*Z*) directions are *3 cm*, *35* μm and *60* μm respectively. A dilute suspension of polystyrene spherical particles with diameter *12* μm *(*ρ_p *= 1.05 (gr/*cm^3*))* dispersed in a suspending fluid composed of deionized water, *0.002* weight per volume (*w/v*) triton X-100 and *0.1 v/v* glycerol is pumped into the channel with a controlled flow rate utilizing a syringe pump from one inlet, accompanied by pumping fluid without particles at an equal flow rate from the second inlet. The volume fraction of particles in the suspension is $\emptyset$ = *0.004*. More concentrated suspensions of $\emptyset$ = *0.011-0.025* are used to study disruption of trains. The flow rate ranges from 85.5 to 342 $\frac{\mu l}{min}$ leading to finite inertia at Re_y *= 30 - 120* inside the channel. Lowering the flow rate below 85.5 $\frac{\mu l}{min}$ does not generate sufficient inertia for a steady-state interparticle spacing. Increasing the flow rate above 342 $\frac{\mu l}{min}$ leads to experimental errors such as delamination of the PDMS from the glass slide, leakage at inlets and alteration of the channel size due to high flow-induced deformation in PDMS microchannels (Dendukuri et al. 2007). The channel configuration allows formation of particle trains at two inertial equilibrium points close to the walls in the *Y* direction for *D = 12* μm particles such that infusing the suspension from one inlet

mainly generates a single train close to one wall. The schematics of the channel are displayed in figure 1. The axial distance between two adjacent particles (d_x) has been computed from recorded snapshots captured using high speed imaging (Phantom V710). The interparticle spacing in multiple sections along the channel has been measured and the values corresponding to the farthest region from the entrance, spanning the last 500 μm section of the channel, have been reported in order to achieve a steady-state spacing.

Computational Method

In this section, a brief explanation of the governing equations, computational parameters and the lattice-Boltzmann method (LBM) which is used to compute particle trajectories in inertial conduit flow is presented. More details about the fundamentals of the lattice-Boltzmann are presented in Ladd (1994) and Nguyen & Ladd (2002), a review article by Aidun & Clausen (2010) and a complete description of Galilean invariance errors due to presence of particles in Clausen & Aidun (2009). The non-dimensional form of the fluid phase governing equations are

$$\boldsymbol{\nabla}.\boldsymbol{u} = 0$$

$$Re\left(\frac{\partial \boldsymbol{u}}{\partial t} + \boldsymbol{u}.\boldsymbol{\nabla}\boldsymbol{u}\right) = -\boldsymbol{\nabla}p + \boldsymbol{\nabla}^2\boldsymbol{u}$$

where length has been non-dimensionalized using the hydraulic diameter h_d, velocity by the average fluid velocity at the channel inlet U and the pressure by ρU^2. The LBM algorithm for hard spherical suspensions, which has been developed by Ladd (1994) with further improvement for moving particles by Aidun, Lu & Ding (1998), is based on the Boltzmann equation for the fluid phase coupled with Newtonian dynamics for solid particles. By computing the force $\boldsymbol{F}_i$ and

torque $\boldsymbol{T}_i$ exerted by the fluid on a particle of mass m_i and moment of inertia I_i, the translational velocity $\boldsymbol{V}_i$ and rotational velocity $\boldsymbol{\omega}_i$ of the particle are calculated as

$$m_i \frac{d\boldsymbol{V}_i}{dt} = \boldsymbol{F}_i$$

$$I_i \frac{d\boldsymbol{\omega}_i}{dt} = \boldsymbol{T}_i$$

In order to calculate particle trajectories in a confined conduit, a rectangular computational box with *128 * 36 * 65* lattice units in *X, Y* and *Z* directions is chosen, where *X* indicates direction of the flow. The rectangular box is periodic in the flow direction and is confined by solid walls in the *Y* and *Z* directions. The specified dimensions of the computational box are chosen in accordance with the dimensions of the microchannel which leads to observation of two equilibrium points close to the walls in the *Y* direction. The resolution of the particles was set at 12.9 lattice units (lu) per diameter. The results of the numerical trajectory analysis were found to be independent of further increase in the resolution by simulating particles with larger size of *D = 16.5 lu* in a 256 * 72 * 130 lu channel. In addition, the results have been examined to be independent of the periodicity in flow direction by iterating some of sample trajectories for a 256 * 36 * 65 lu box.

Results and discussion

In figure 2, the probability density functions (pdf) of d_x for Re_p = 2.8, 5.6 and 8.3 are presented. The highest peak in the pdf corresponds to the most probable spacing between two consecutive particles at a certain Re_p. Although the adverse effect of particle sedimentation was minimized by matching the density of particles and the fluid, fluctuation in the number of particles observed in each imaging snapshot is inevitable. Considering that the concentration of suspensions used

for inertial self-assembly applications is small *($\emptyset$ < O(0.01)),* the *average length fraction* defined as $<L_f>$ = $<N>D/L$, where $<N>$ is the average number of particles per frame monitored throughout the experiment and L is the frame length(500 μm in the present study) can be used as a replacement for volume fraction $\emptyset$ (Di Carlo (2009)). The average length fraction $<L_f>$ is a direct measure for proximity between particles which affects hydrodynamic interactions. In the experimental measurements discussed here, d_x is compared in trains with identical $<L_f>$. This approach assists in differentiating the influence of Re_p on spacing from possible effects of fluctuations in the number of particles in trains. In the probability density functions of figure 2 the value of $<L_f>$ is *0.1*. It is observed in figure 2 that for Re_p = 2.8 the preferred spacing, which corresponds to the peak in the pdf curves, forms around *5D* and for high Re_p of *8.3*, the preferred spacing is located around *2.5D*. When varying Re_p no intermediate preferred spacing is observed and peaks of the pdf are consistently observed around *2.5D* and *5D*.

Although infusing the suspension from a separate inlet increases the probability of forming one train with axial alignment of particles, i.e. axial ordering, a small number of particles may migrate towards the opposite wall. Sporadic migration of particles towards the opposite wall can start at the channel inlet and during merging. Two consecutive particles which are located on opposite sides of the channel form a lateral ordered pair. The peaks observed in the pdf curves correspond to the spacing between consecutive particles, without distinguishing between axial and lateral ordered pairs. To make a distinction between axial and lateral orientations, the spatial probability distribution of neighboring particles are presented in figure 3. The spatial probability distribution, p(**r**), is obtained by constructing a histogram around each particle which is populated by the location of adjacent particles. The histogram is normalized by the total number

of samplings. Considering that the pair orientation vector is used to construct the histograms, the distributions span the entire space around the reference particle, including negative **X** and **Y** values; although the probability of occupying negative locations is not significant. It is observed in figure 3 that at Re_p= *2.8*, particle pairs with axial ordering ($\Delta Y = 0$) equilibrate close to $d_x \sim 5D$. With increasing inertia to Re_p= *8.3*, the preferred spacing between particles forms around *2.5D*. In the spatial representation of p(**r**) at Re_p= *2.8*, a secondary zone at $d_x \sim 2.5D$ is also seen due to the lateral pair configuration ($\Delta Y \neq 0$) which results in the formation of a secondary peak around *2.5D* in the probability density functions of figure 2. The spacing between particles with lateral ordering has been predominantly observed around *2.5D* for all Re_p studied.

Humphry et al. (2010) measured the axial spacing between particles in single inlet channels and reported $d_x \sim 2.2D$; mainly for suspensions flowing at $Re_p \sim$ O(1) in microchannels. Considering that inertial flow of a dilute suspension in a single inlet channel leads to formation of particle trains close to both walls, the probability of observing lateral ordering increases. Therefore, an axial spacing of *2.2D* between particles, agrees well with our results.

Experimental observation of interparticle spacing at preferred axial locations of $d_x \sim 2.5D$ and *5D* can be further investigated using numerical simulations of particle relative motions. The classes of relative motion of particles in a dilute suspension can be assembled from trajectories of isolated pairs of particles (Haddadi & Morris 2014). Pair trajectories are obtained by calculating the trajectory of one particle with respect to the coordinate frame located at the center of mass of the second particle. The lattice-Boltzmann method has been utilized for studying trajectories,

which has been proven to be an efficient technique for numerical simulation of inertial suspension flow. The evolution of sample pair trajectories until reaching a steady-state separation at Re_p= *2.8* and *8.3* is demonstrated in figure 4. To identify the most probable pair separation at each Re_p, the steady-state separation of pair trajectories with various initial configurations has been examined numerically. A Large number of initial configurations, composed of *107* pair orientations for each Re_p, have been simulated to construct a thorough representation of the relative motions. The steady-state pair separations are used to populate a spatial histogram which is constructed around the reference particle. The spatial probability densities of pair equilibrium separations for Re_p = 2.8 and *8.3* are shown in figure 5 (a) and (b) respectively. It is seen that at Re_p= *2.8* and for all initial configurations, the most probable spacing for an axially ordered pair is located at *5D*. For pairs with lateral orientation, the preferred spacing forms at d_x = *2.5D*. At Re_p= *8.3*, axially ordered spacings at *2.5D* and *5D* are more pronounced, where the probability of reaching an equilibrium at *2.5D* is significantly higher. In addition, pairs with lateral ordering tend to equilibrate at *2.5D* from the reference particle for all Re_pvalues.

The match between preferred spacings observed in experiments (figures 2 and 3) and the steady-state separations between pairs in numerical simulations (figure 5) implies that a finite number of *attractors* contribute to formation of preferred interparticle spacings in trains. The attractor with highest probability at low Re_p is located at *5D*. With increasing Re_p, rather than a gradual shift in the location of the attractors, the probability of the *5D* attractor decreases and the *2.5D* attractor becomes more probable. Using numerical simulations of the disturbance streamlines around a single force-free particle moving in a rectangular channel, the equilibrium distance

between two particles has been related to formation of closed-streamline regions adjacent to the particle (Humphry et al. 2010). Considering that the disturbance streamlines around a single particle are affected by the presence of other particles, the fundamental description of the flow leading to formation of attractors remains an open question. It should be noted that pair trajectory attractors are not particular to confined inertial flows and have also been observed in the relative motion of particles in Stokes flow of dilute suspensions in two dimensional microchannels, where linearity of Stokes flow governing equations allows analytical progress (Uspal & Doyle 2012). It should be emphasized that in the present work, the location of the attractors in the pair trajectory space is obtained from numerical sampling of the pair motion. Although a large number of initial pair configurations have been simulated to calculate the location of attractors, making a definite conclusion about the total number and location of pair trajectory attractors is not possible. However, the combination of experimental observations and numerical sampling of the pair space corroborates existence of preferred spacings between adjacent particles at each Re_p. We also note that there is a deviation (between *0.2-0.4D* for the location of the preferred spacings) from the *2.5D* and *5D* attractors in experimental measurements. This deviation may be due to unavoidable experimental limitations, including pixel size accuracy in image processing, dispersion in particle size distributions and presence of multiple particles in a train (more than an isolated pair), which does not exist in simulations of an isolated pair.

The question arises of whether the locations of the attractors depend strongly on the channel and particle size or are more generally observed. The generality has been examined for selected particle sizes and dimensions of the channel cross section. The location of the attractors are measured for Re_p = *2.8* and *8.3*, where the preferred spacing for $D = 12\ \mu m$ in λ= 0.58 channels

has been previously explained to be respectively around *5D* and *2.5D*. Similarly, for *D = 4.8* and 20 μm particles in λ = 0.58 channels the location of the attractors remained unchanged. Identically, for *D* = 12 and 20 μm in λ = 1 channel ($l_y = l_z$ = 60 μm), the attractors at Re_p = *2.8* and *8.3* form around *60* μm and 30 μm.

For inertial self-assembly of particles in trains, in addition to Re_p, the average length fraction of particles <L_f> in trains is another important parameter. Attaining a tangible increase of length fraction is achieved by increasing the volume fraction ∅ to *O(0.01)*. It has been shown that increasing ∅, leads to formation of multiple trains in microchannels with large aspect ratios of the channel cross section (Humphry et al. (2010)). In order to study the spacing between particles for a more concentrated suspension, experiments have been conducted at ∅ = *0.011 - 0.025*, which results in <L_f> ~ *0.3 - 0.6*. (It should be noted that <L_f> = *0.1* is achieved at ∅ = *0.004*). The volume fraction of suspensions is still considered to be in a dilute rheological regime, however increasing ∅ to *O(0.01)* leads to a pronounced increase of <L_f> to *0.6* which can alter dynamic self-assembly of particles into trains. Numerical simulations have also been conducted and the average distance between pairs of consecutive particles versus time has been monitored. Figure 6(a) shows numerical values of <d_x> versus dimensionless time t^* = t<U>/D (<U> is the average inlet velocity) at Re_p = *2.8*, which includes snapshots taken from experimental measurements. For numerical simulations of larger <L_f>, the number of particles in the computational box has been increased without changing the box size. The average distance between particles in *X* and *Z* directions, denoted as <d_x> and <d_z> respectively, are computed as the average center of mass separation of particle pairs in each time step. It is observed that with increasing <L_f> to 0.3 (three times higher than previous results) the preferred axial spacing

decreases to *3.2 D* from the previously observed *5D* for $<L_f>$ ~0.1. Although at $<L_f>$ ~ 0.3 particles are still self-assembled into ordered trains and the final $<d_x>$ reaches a steady value, with further increase of $<L_f>$ to 0.6 interparticle distance starts to fluctuate which prevents formation of a self-assembled train; as it can be seen in experimental snapshots. The disruption of trains can be viewed from fluctuations of spacing in either *y* or *z* directions computed numerically. Figure 6(b) exhibits $<d_z>$ for $<L_f>$ = *0.3* and *0.6*, where apparent temporal fluctuations in spacing and disruption of particle ordering is seen at $<L_f>$ = *0.6.*

Figure 7 shows reversing zone between pair of 12 micron particles in a train visualized for the first time using 2 micron tracer particles and we hypothesize that trajectory attractors, reduced spacing, and disruption of trains happen because of the changes in reversing zone. More comprehensive numerical work is needed to investigate this phenomenon.

Application:

Controlling number of particles/cells in droplets for single-cell assays (without jetting)

One of the established systems used for droplet generation is "flow focusing"; where cross flow of oil causes pinch off and droplets form. However, these systems are very sensitive to flow rates (require expensive and bulky pumps), and a slight change in the flow rates could cause change in droplet size and jetting (Unlike droplet generator that I have developed presented in chapter 3,4). Usually the flow rates used in these systems are very low to avoid jetting. Here we show how using the reported attractors in inertial flows we could control number of particles/cells per droplet. For single-cell studies we need to have one cell per droplet. Therefore if the droplet generation is higher than the time that takes for the second particles in a pair or train of particles

to reach breakup junction, then we avoid having more than one cell/particle per droplet. The first challenge here is that since we need to operate at high flow rates to control interparticle spacings, then we get jetting in the droplet formation device. We addressed this challenge by increasing nozzle dimension (width) compared to our channel to see if we can control the jetting (figure 8) by reducing oil and fluid velocities at the droplet formation junction (previous works have reported that high velocity of oil and fluid leads to jetting). We found out that if the nozzle width is higher than the width of the original channel, then we can go to much higher flow rates that people have reported before without getting jetting. In figure 9 the dimension of the device for controlling the jetting and encapsulation is shown. We could go up to flow rate of 24 $\mu l/min$ and the each of the oil flow rates is 30 $\mu l/min$. We could also go to 40 $\mu l/min$ for the water flow rate by using nozzle width of 95 micron. As was reported in previous section, based on this flow rate we observe preferred spacing at 5D (around 60 μm). We tested HL60 and PC3 cell lines and although cells are deformable and are not completely spherical, interestingly we still observe preferred spacing at 60 μm for those cell lines. Figure 10 shows snapshot of droplet encapsulation of the beads and cells in separate experiments. As it is shown we do not see more than one cell per droplet because the frequency of droplet generation is high enough so that when the first particle reaches the breakup junction, before reaching the second particle/cell (60 μm far from the first one) at least one droplet is generated and the two will not be in the same droplet. This technique and geometry could potentially be used for encapsulating for example two cells/particles per drop if the droplet generation frequency is controlled accurately for different applications. We also observe same preferred spacings for cells and particles at higher flow rates (Re=90), shown in figure 11.

Conclusion

The experimental measurements of the distance between consecutive particles self-assembled in trains, which have been validated by numerical simulations, can be used as a predictive model for dynamic self-assembly of particles with precise separations from one another. Depending on the Re_p, the most probable spacings in a dilute regime of $\emptyset$ = *O(0.001),* corresponding to ``trajectory attractors", are located around *2.5D* and *5D*. The attractors appear to be generally observed for varying ratios of particle size to channel dimensions and channel aspect ratios, although a more exhaustive investigation of the space would be required to confirm this result. By increasing the concentration of suspensions to $\emptyset$ = *O(0.01),* the spacing between particles decreases until reaching an unsteady state spacing where focusing the particles into trains is no longer possible. The results could be helpful in practical applications, suggesting the ability to make use of either of the two attractors for controlled encapsulation of particles/cells in droplets in a modified flow focusing droplet generator without having jetting.

Acknowledgement

The support from ONR Young Investigator Program is acknowledged. We would like to thank Professor Anthony Ladd at University of Florida-Gainesville for providing the initial lattice-Boltzmann solver.

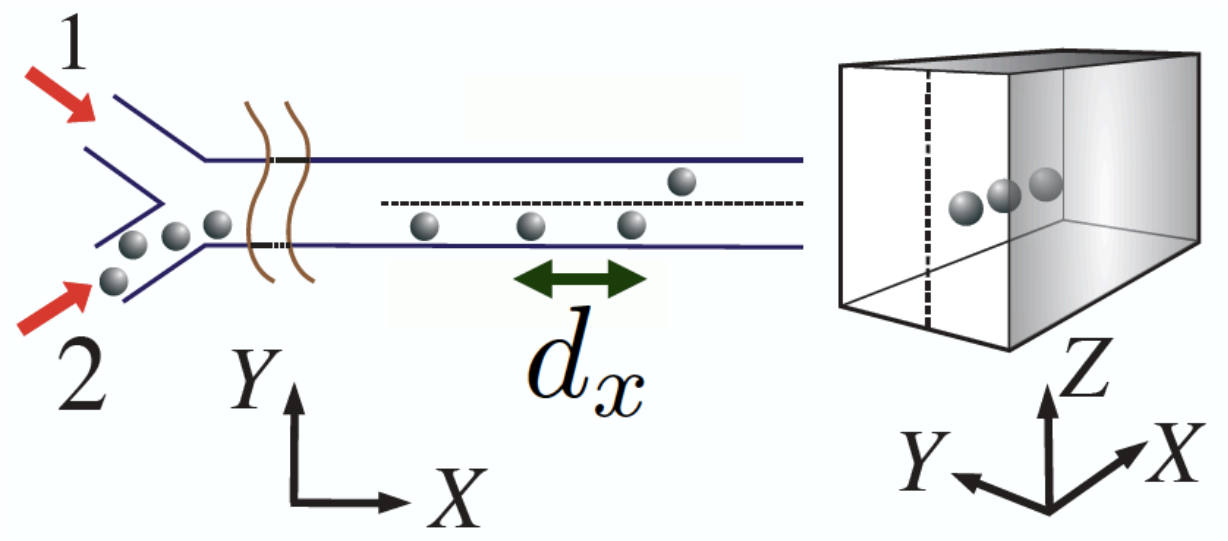

Figure 1: Schematic of the channel with two inlets utilized for particle self-assembly into one train. A particle suspension is pumped from one inlet and fluid without particles is infused from the opposite inlet. Dimensions of the channel in the X (flow), Y (lateral) and Z (transverse) directions are 3cm, 35 micron and 60 micron respectively, which leads to formation of two inertial focusing positions near the walls in the Y direction.

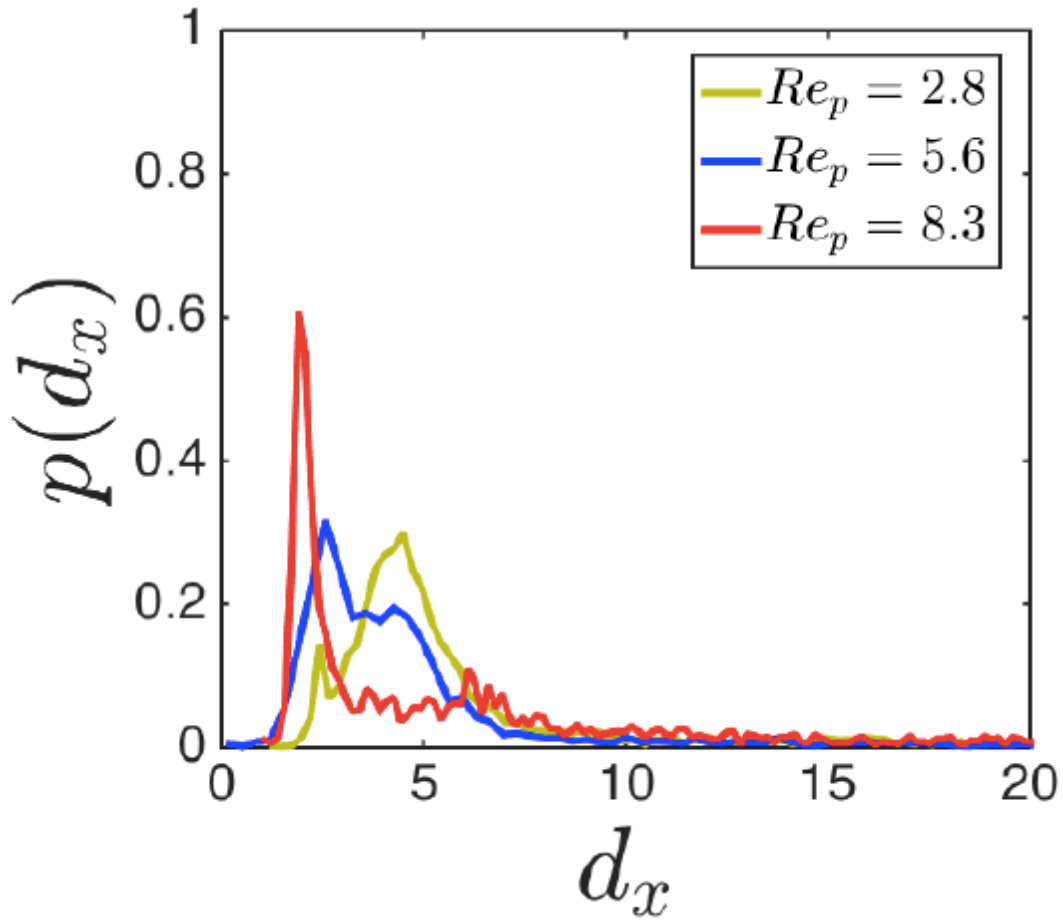

Figure 2: The probability density functions (pdf) of axial spacing between particles, dx, for Rep = 2.8; 5.6 and 8.3 (corresponding to Rec = 30, 60 and 90). The aspect ratio of the channel cross section is ly/lz= 0.58 and the particle diameter is D = 12 micron. With a slight deviation (< 0.4D), formation of most probable spacings around 2.5D and 5D are observed as the modes (highest peaks) in the pdf.

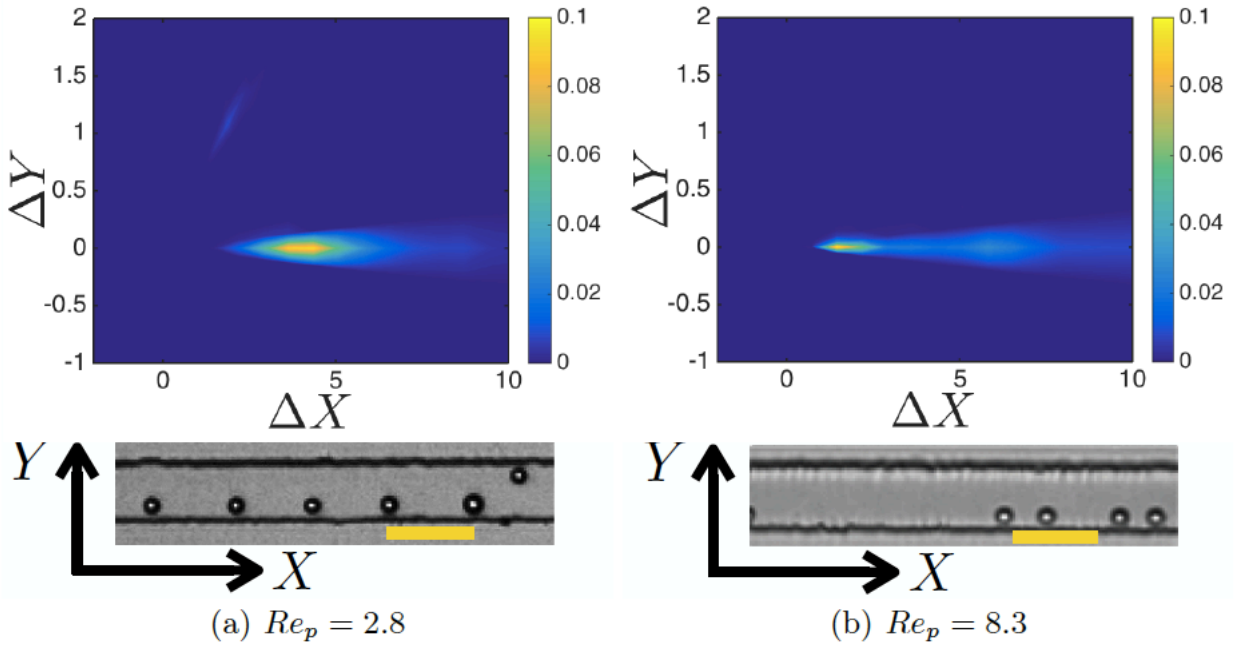

Figure 3: The spatial probability distribution of finding the adjacent particle in the vicinity of a reference particle p(r) at (a) Rep = 2.8 and (b) Rep = 8.3. A streak of low probability which is observed at $\Delta X \sim 2.5D$ and $\Delta Y \sim 1.2D$ corresponds to laterally ordered pairs of particles. Snapshots taken from experiments are included to exhibit the self-assembled trains (scale bar shows a length of 60 micron).

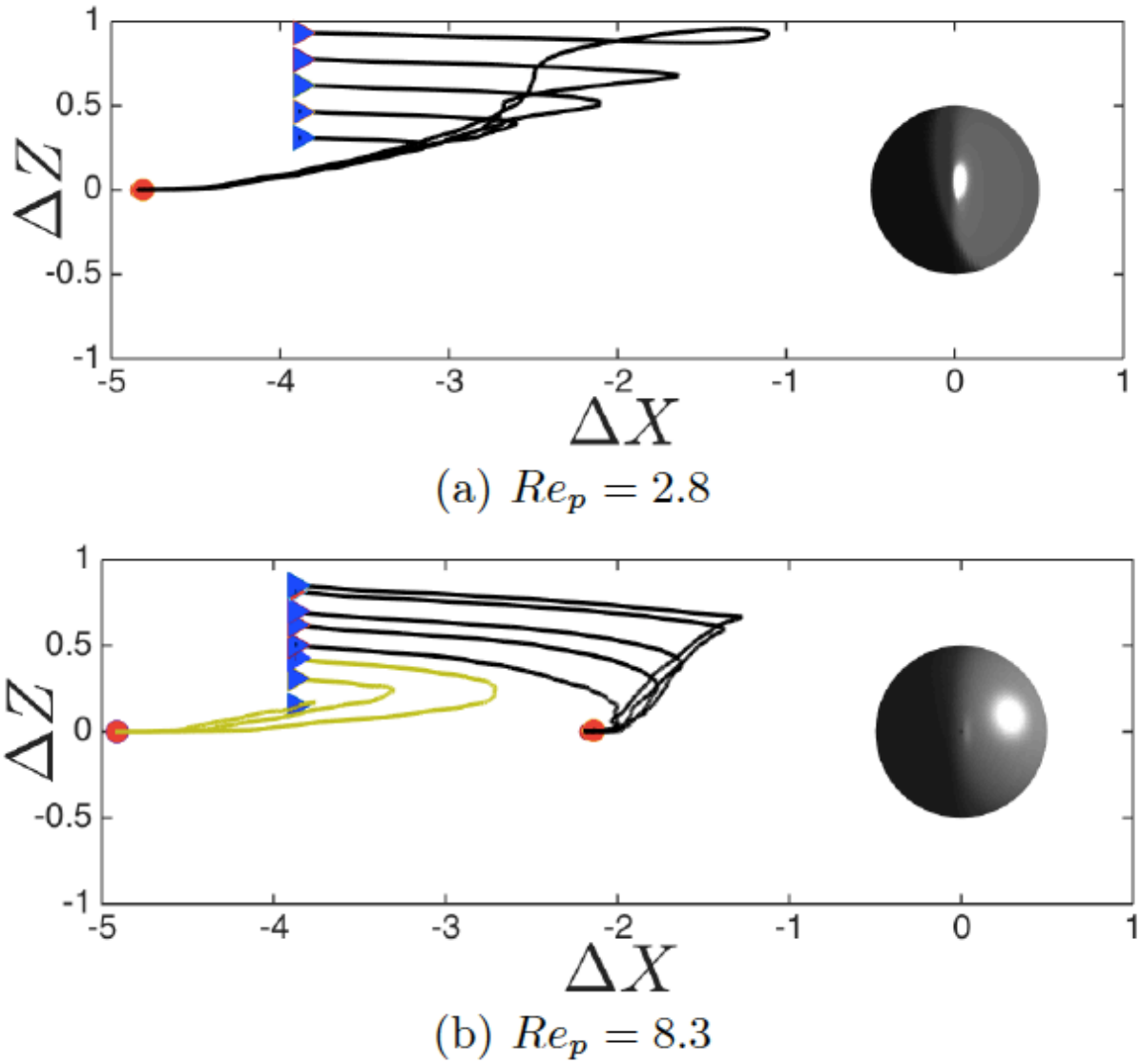

Figure 4: Selected pair trajectories calculated numerically at (a) Rep = 2.8 and (b) Rep = 8.3 projected on the XZ plane. Blue triangles correspond to the starting points of the second particle relative to the reference particle shown at the origin and red circles correspond to the final steady-state separations.

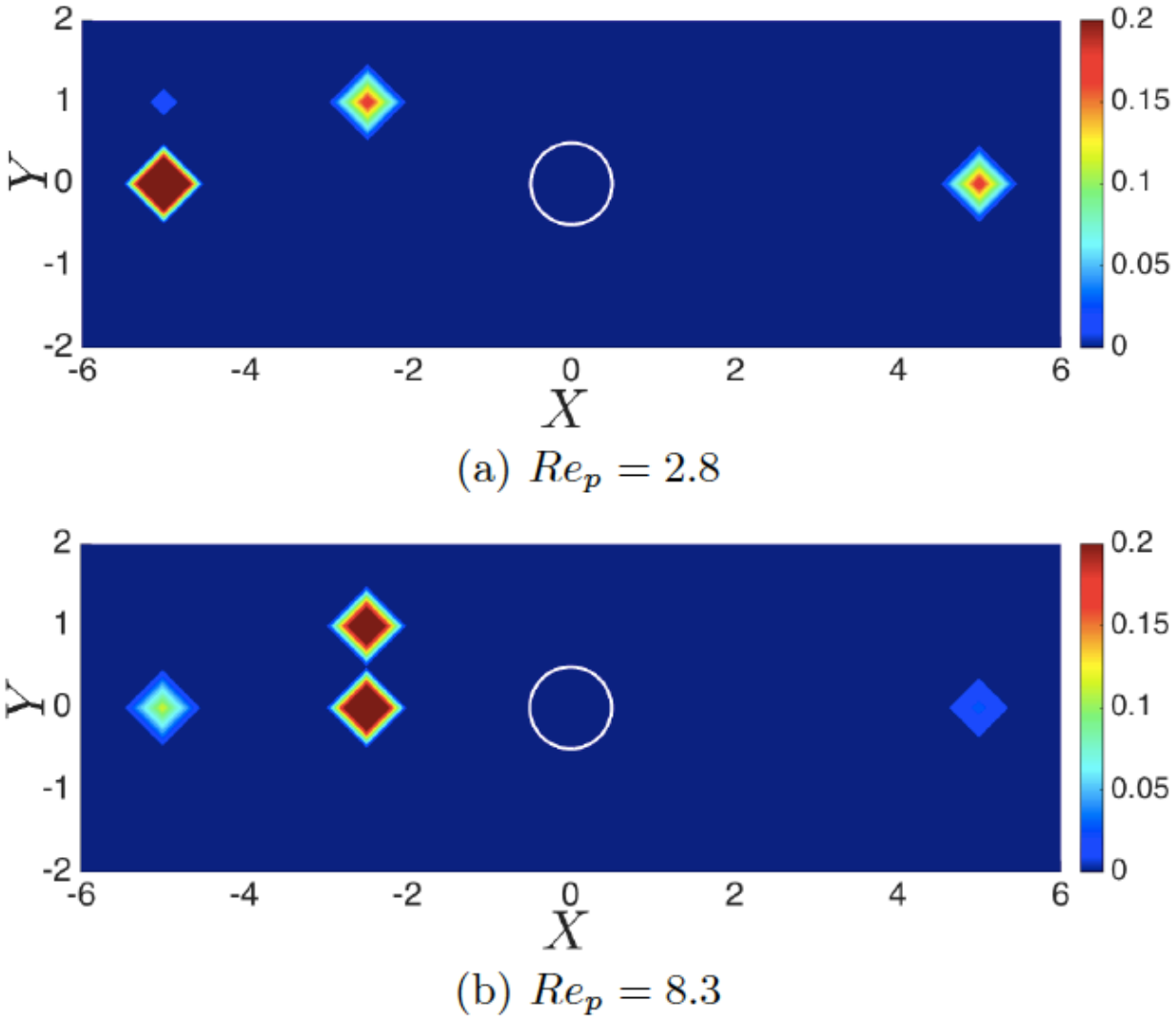

Figure 5: Attractors at preferred spacings and their probabilities, calculated by simulating the motion of pairs starting from various initial con_gurations at (a) Rep = 2.8 and (b) Rep = 8.3. The boundary of the reference particle is also indicated in the figure. The figure comprise attractors forming in axial and lateral directions. Attractors form at 5D and 2.5D, and the most probable axial attractors are located at 5D for Rep = 2.8 and 2.5D for Rep = 8.3. Attractors of lateral orientation are located at 2.5D for both Rep values.

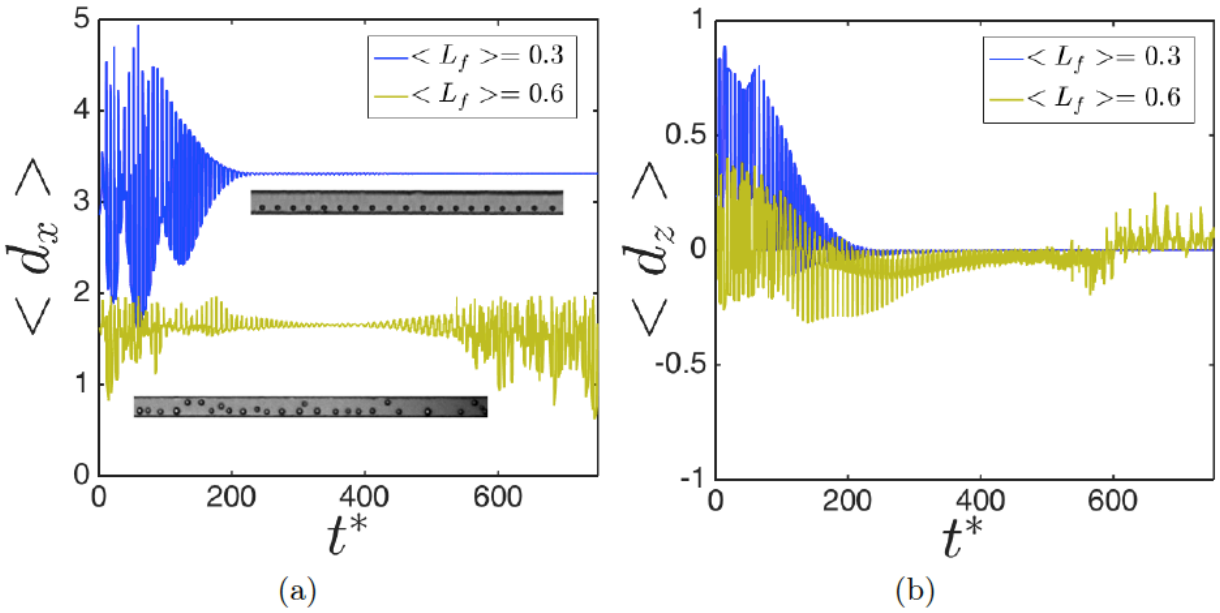

Figure 6: Variation of average spacing between particles versus time for larger concentrations of particles: (a) Average axial separation < dx > at Rep = 2.8 and (b) simulation results showing average transverse separation < dz > at Rep = 2.8. Dimensionless time is defined as t<U>/D .

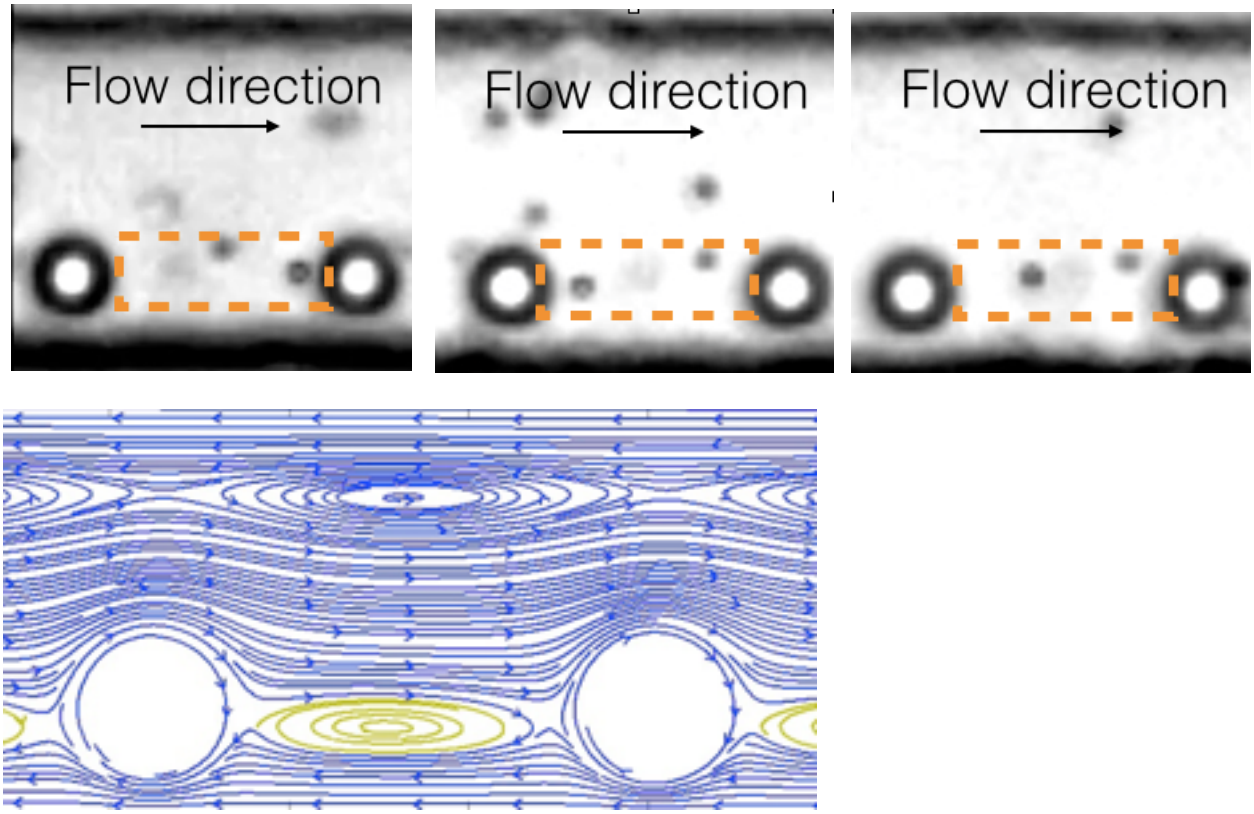

Figure 7: 1 micron tracer particle is used for visualization of the reversing streamlines zone between pair of particles in a train for the first time. Bottom figure is showing streamlines using a lattice Boltzmann simulation (yellow shows reversing zone)

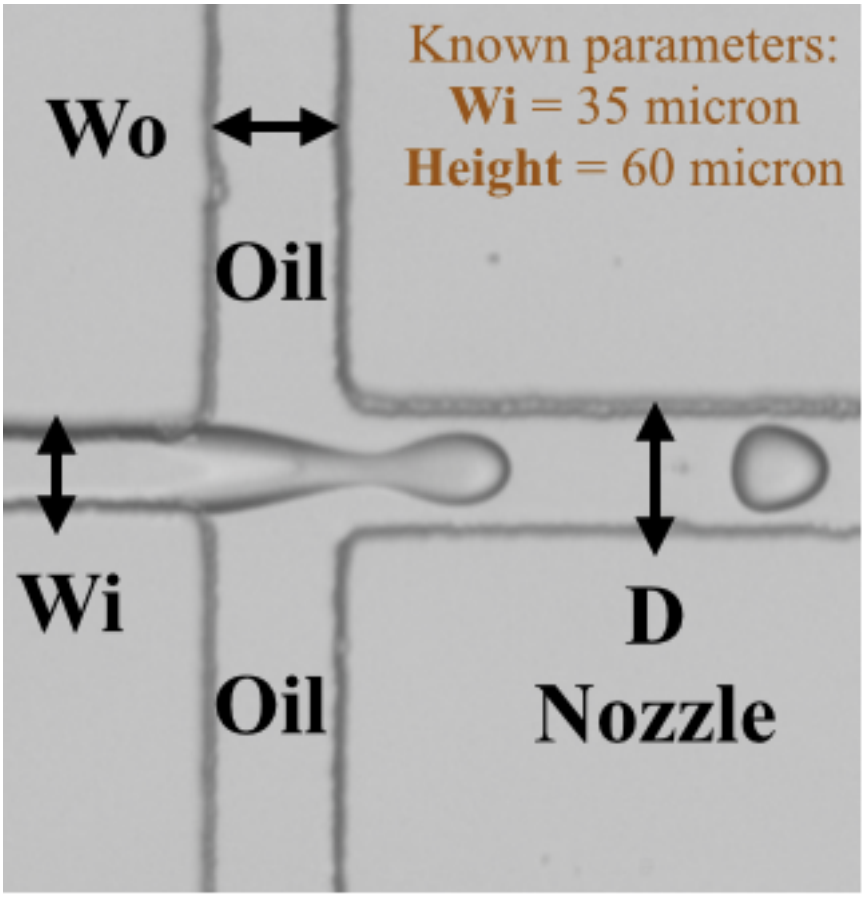

Figure 8: Different parameters in the flow focusing design. Our goal is to avoid jetting at high fluid flow rates by increasing nozzle width (D), which locally reduces fluid and oil velocities (which have been reported previously that cause jetting)

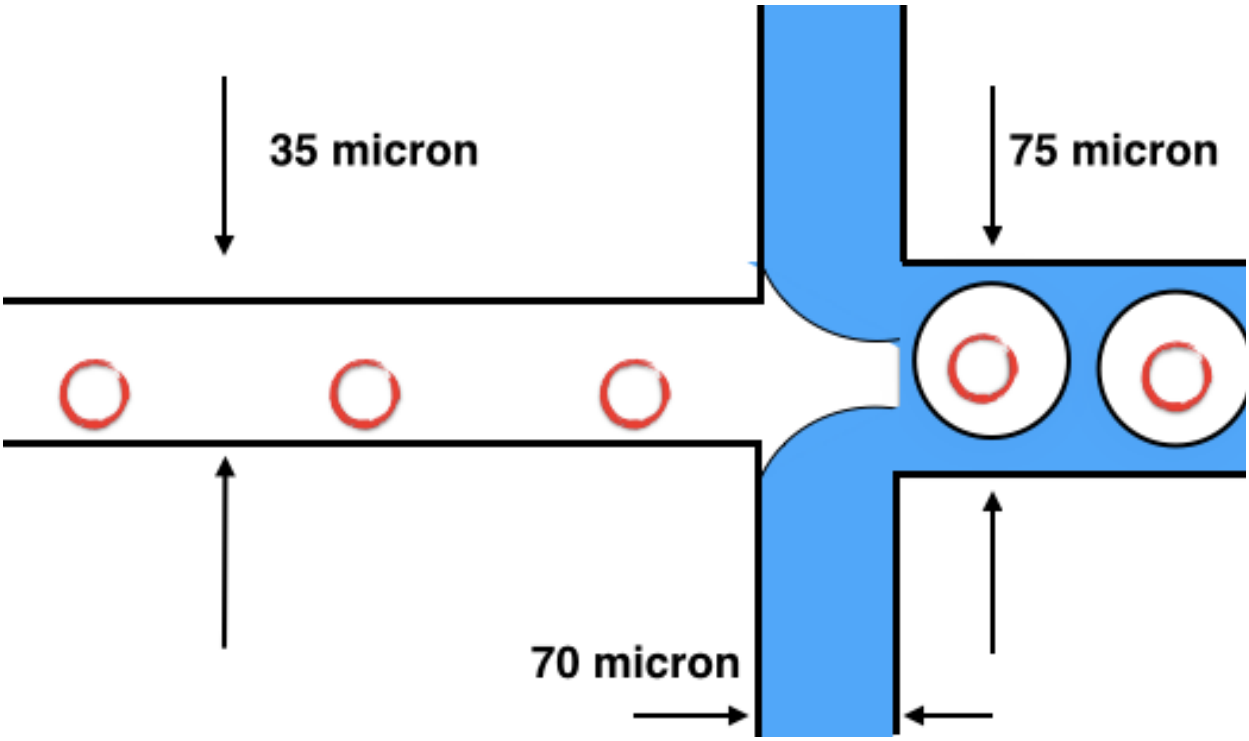

Figure 9: Schematic of the flow focusing design that is used for high-flow rate encapsulation without jetting.

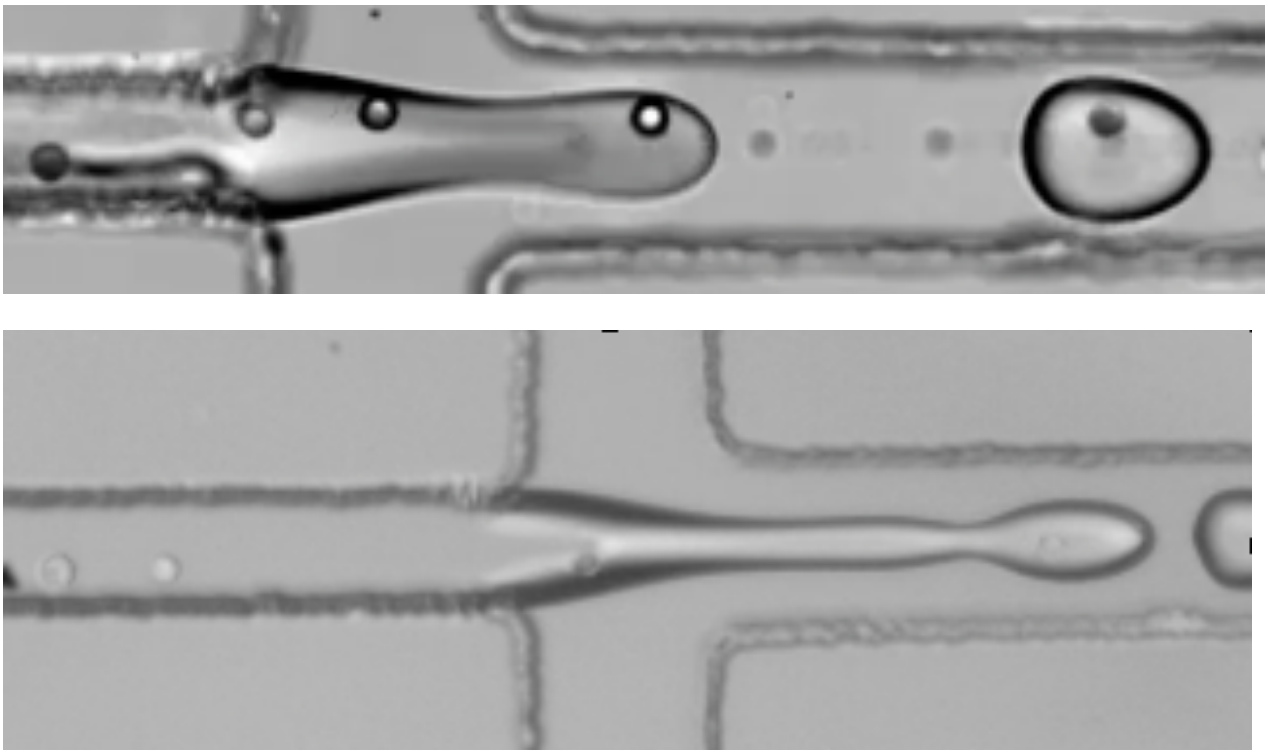

Figure 10: Controlled encapsulation at high flow rates. A) particles (20 microliter /min) B) PC3 Cells (25 microliter/min). Oil flow rate is 30 microliter/min.

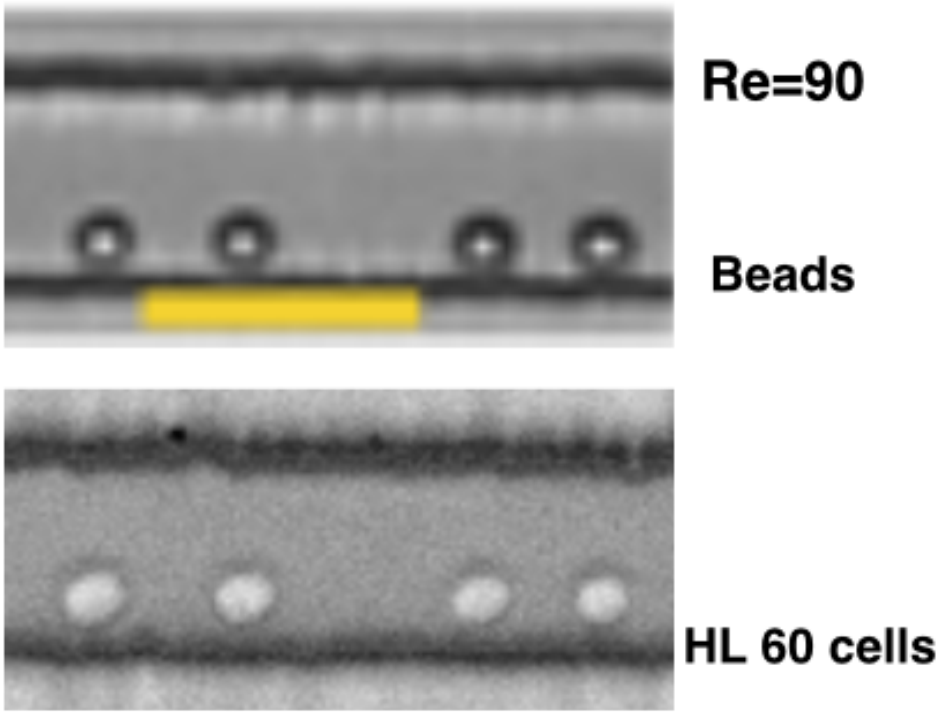

Figure 11: Preferred spacing is observed at same distance for beads and cells although cells are deformable and not completely spherical.

Supplementary figures:

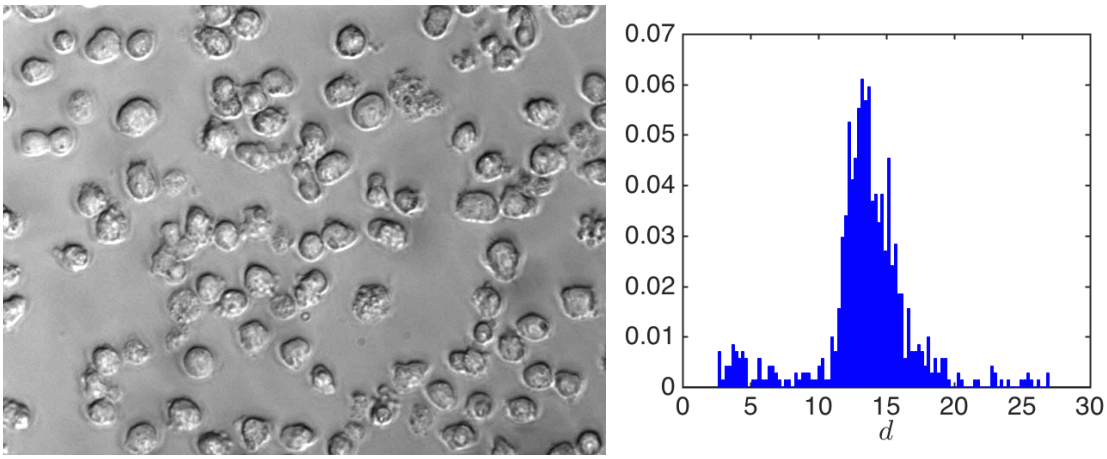

Supplementary figure 1: HL 60 cells

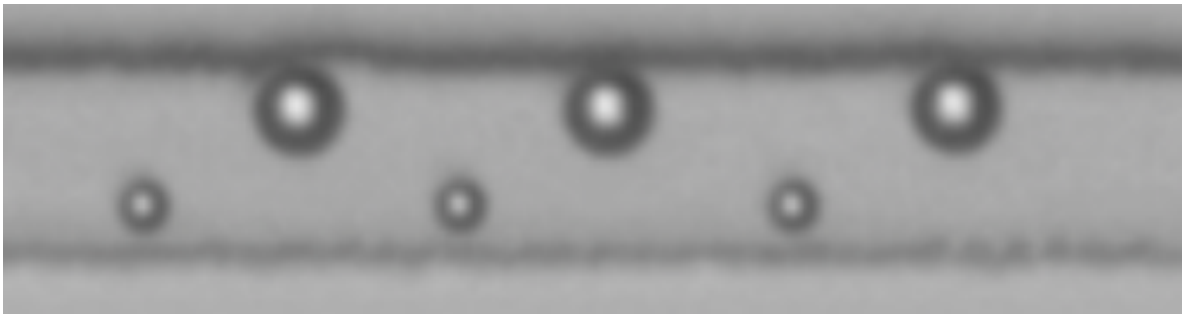

Supplementary figure 2: Encapsulation can also be done for self-assembled bidisperse suspensions, which is very valuable for drop-seq application (droplet sequencing). We used a 2 inlet device and from top inlet we had 20 micron particles and from bottom inlet we had 10 micron particles. Either of those could be replaced by cell suspension similar to drop-seq where one cell and one drop shoud be encapsulated in a drop.

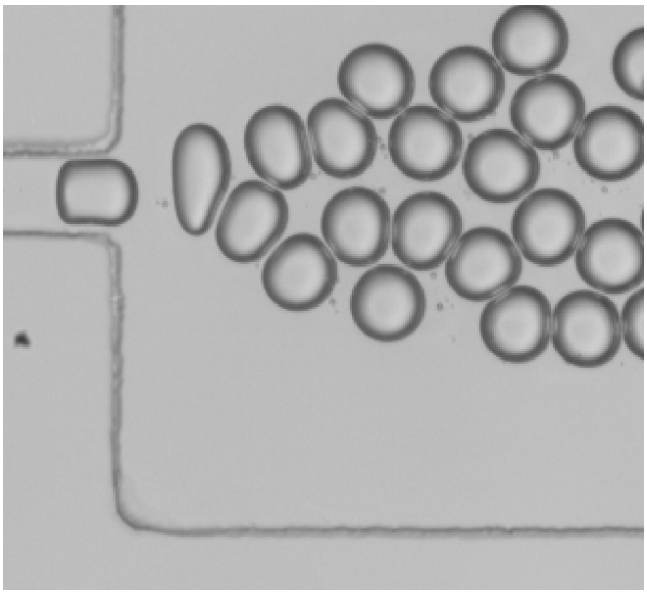

Supplementary figure 3: Generated droplets

References:

1. AIDUN, C. K. & CLAUSEN, J. R. 2010 Lattice-Boltzmann method for complex flows. Annu. Rev. Fluid Mech. 42, 439-472.

2. AIDUN, C.K., LU, Y. & DING, E. 1998 Direct analysis of particulate suspensions with inertia using the discrete Boltzmann equation. J. Fluid Mech. 373, 287-311.

3. AMINI, H., LEE, W. & DI CARLO, D. 2014 Inertial microfluidic physics. Lab Chip. 14, 2739-2761.

4. ASMOLOV, E.S. 1999 The inertial lift on a spherical particle in a plane Poiseuille flow at large channel Reynolds number. J. Fluid Mech. 381, 63-87.

5. CHUN, B. & LADD, A.J.C. 2006 Inertial migration of neutrally buoyant particles in a square duct: An investigation of multiple equilibrium positions. Phys. Fluids. 18, 031704.

6. CLAUSEN, J.R. & AIDUN, C.K. 2009 Galilean invariance in the lattice-Boltzmann method and
its effect on the calculation of rheological properties in suspensions. Int. J. Multiphase Flow. 35, 307-311.

7. DI CARLO, D. 2009 Inertial microfluidics. Lab Chip. 9, 3038-3046.

8. DI CARLO, D., EDD, J.F., HUMPHRY, K.J., STONE, H.A. & TONER, M. 2009 Particle segregation and dynamics in confined flows. Phys. Rev. Lett. 102, 094503.

9. DI CARLO, D., IRIMIA, D., TOMPKINS, R.G. & TONER, M. 2007 Continuous inertial focusing, ordering, and separation of particles in microchannels. Proc. Natl. Acad. Sci. U.S.A. 104, 18892-18897.

10. DUFFY, D.C., MCDONALD, C.J., SCHUELLER, O.J.A. & WHITESIDES, G.M. 1998 Rapid
prototyping of microfluidic systems in poly (dimethylsiloxane). Anal. Chem. 70, 4974-4984.

11. EDD, J.F., DI CARLO, D., HUMPHRY, K.J., KOSTER, S., IRIMIA, D., WEITZ, D.A. & TONER, M. 2008 Controlled encapsulation of single-cells into monodisperse picolitre drops. Lab Chip. 8, 1262-1264.

12. HADDADI, H. & MORRIS, J.F. 2014 Microstructure and rheology of finite inertia neutrally buoyant suspensions. J. Fluid Mech. 749, 431-459.

13. HADDADI, H. & MORRIS, J.F. 2015 Topology of pair-sphere trajectories in finite inertia suspension shear flow and its effects on microstructure and rheology. Phys. Fluids. 27, 043302.

14. HO, B.P. & LEAL, L.G. 1976 Migration of rigid spheres in a two-dimensional unidirectional shear flow of a second-order fluid. J. Fluid Mech. 76, 783-799.

15. HOOD, K., LEE, S. & ROPER, M. 2015 Inertial migration of a rigid sphere in three-dimensional Poiseuille flow. J. Fluid Mech. 765, 452-479.

16. HUMPHRY, K.J., KULKARNI, P.M., WEITZ, D.A., MORRIS, J.F. & STONE, H.A. 2010 Axial and lateral particle ordering in finite Reynolds number channel flows. Phys. Fluids. 22, 081703.

17. HUR, S.C., TSE, H.T.K. & DI CARLO, D. 2010 Sheathless inertial cell ordering for extreme throughput flow cytometry. Lab Chip. 10, 274-280

18. LADD, A.J.C. 1994a Numerical simulations of particulate suspensions via a discretized Boltzmann equation. Part 1. Theoretical foundation. J. Fluid Mech. 271, 285-309.

19. LADD, A.J.C. 1994b Numerical simulations of particulate suspensions via a discretized Boltzmann equation. Part 2. Numerical results. J. Fluid Mech. 271, 311-339.

20. LEE, W., AMINI, H., STONE, H.A. & DI CARLO, D. 2010 Dynamic self-assembly and control of microfluidic particle crystals. Proc. Natl. Acad. Sci. U.S.A. 107, 22413-22418.

21. MARTEL, J. & TONER, M. 2014 Inertial focusing in microfluidics. Annu. Rev. Biomed.

Eng.16, 371-396.

22. MATAS, J.P., GLEZER, V., GUAZZELLI, E. & MORRIS, J.F. 2004 Trains of particles in finite-Reynolds-number pipe ow. Phys. Fluids. 16, 4192-4195.

23. NGUYEN, N. Q. & Ladd, A. J. C. 2002 Lubrication corrections for lattice-Boltzmann simulations of particle suspensions. Phys. Rev. E: Stat. Phys., Plasmas, Fluids. 66, 046708.

24. SEGRE, G. & SILBERBERG, A. 1961 Radial particle displacements in Poiseuille flow of suspensions. Nature. 189, 209-210.

25. USPAL, W.E. & DOYLE, P.S. 2012 Collective dynamics of small clusters of particles owing in a quasi-two-dimensional microchannel. Soft Matter. 8, 10676-10686.

Chapter 3

Magnetic droplet generator for point-of-care applications

Abstract

We present a microfluidic droplet generation technique, where instead of pumps, only magnetic field gradients adjusted by the position of an external magnet are used for controllable emulsification of ferrofluid containing solutions. Uniform droplet generation at frequencies O(1−100)Hz per channel for long periods of time (10s of minutes) were easily achieved. In this method, adding magnetic nanoparticles (10nm) into aqueous solutions imparts a magnetic body force on the fluid in the presence of an external magnetic field gradient. Consequently, the aqueous fluid moves toward the position of an external magnet and towards a junction with a larger width and height oil filled reservoir. Emulsification occurs at the junction due to a rapid change in surface tension forces due to the abrupt change in channel height. Droplet generation rate could be controlled by adjusting surface tension/viscosity, number of channels, and strength of the magnetic force. The geometry of the channel, rather than flow rates or magnetic force, plays the dominant role in defining the droplet size. In addition, reagents mixed with ferrofluids could also be introduced from two or more separate inlets and mixed prior to emulsification as they move toward the step driven by magnetic force. Mixing reagents on chip and forming droplets all within a small foot-print defined by movement of an external magnet is a unique feature of this method suitable for point-of-care diagnostics and other bioengineering applications.

Introduction

Droplet or digital microfluidics has been a versatile tool for a range of applications such as genome profiling and high throughput digital assays in recent years[1-5]. Discrete droplets can be used to compartmentalize volumes and perform assays on single entities (digital assays), as microreactors for controlling reactions over time with reduced diffusion, for controlled delivery and release of oxygen and drugs[6], for synthesis of microstructured materials[7], for encapsulating ordered particles and cells[8,9] and a multitude of other applications. Many digital assays, such as digital PCR and ELISA, have transitioned to commercial products, however, the mechanism of forming arrays of drops using bulky pressure driven or syringe pump driven flow systems has limited the ability to extend such assays to point of care formats for new digital diagnostic assays. There is still a significant need for controllable small footprint point-of-care and stable droplet generation approaches.

Previously, droplet formation in microchannels has been mainly achieved using flow focusing[10] coflow[11], T-junction[12-14] and step emulsification combined with cross flow/co-flow techniques[15-18]. Most of these methods operate at relatively low flow rates for stable droplet generation. Controlling droplet generation frequency without changing droplet size is also not easily achieved in these methods, because of the sensitivity to flow rates, flow rate ratios, and the pumps involved. Droplet generation driven by a gradient of confinement is also another method for high-throughput droplet generation[19] which has the advantage of not requiring an additional flow of continuous phase. Still the technique requires flow rate control using pumps if multiple solutions are to be introduced with known ratios to form a final controlled drop for downstream

reaction. Step emulsification devices on disk have also been used for droplet formation[20,21]. Pumping can be achieved by rotation of the disk-shaped chip in those devices.

Recently, ferrofluids, fluids that contain suspended magnetic nanoparticles, have been used in many biomedical applications[22], for example as a tool for adjusting the size of droplets when magnetic fluids are applied in the T-junction and flow focusing droplet generators[23-25] . For example Liu et al.[26] have studied formation of ferrofluid droplets, velocity field and droplet size in a pressure driven flow focusing device under influence of uniform magnetic field. Tan et al.[27] have also studied the effect of an external magnet (and also magnetic flux density gradient) and flow rates on droplet size in a pressure driven T-junction droplet generator. However, a need for accurate pumps for droplet generation in these pressure driven systems limits applying these droplet generators as portable devices for point-of-care applications.

Addressing these challenges, here, we demonstrate a new technique for droplet formation based on magnet-induced flow of ferrofluid in a step emulsification device that operates without any pumps. The ability to quickly change the droplet generation rate by adjusting the magnetic field through the location of the external permanent magnet is a unique feature of this system. We demonstrate droplet generation by using only a small external magnet (figure 1). Because the technique does not require a co-flowing continuous phase for break-up, a parallelized version of the device is easily achieved (Figure 1A-B). By using 10 channels connecting the inlet to the continuous-phase reservoir we obtained an average droplet generation rate up to ~800 droplets per second. Further parallelization could increase generation rate even further (on the order of millions of droplets per second). We found that dimensions of the channel are the dominant

parameters in controlling droplet size, rather than other parameters such as magnetic field strength and surface tension. We also demonstrated mixing of reagents on chip prior to encapsulation in droplets. Fluids (both containing magnetic nanoparticles) are co-flowed on chip as they move toward the permanent magnet and droplets containing both fluids will form after reagents pass the step junction. This promises to be an important feature for point-of-care applications, which could be enabled using this new emulsification approach.

Materials and methods

Device fabrication

The device is fabricated based on the conventional protocols for making PDMS (polydimethylsiloxane- SYLGARD 184 silicone elastomer kit, Dow Corning Corporation) channels[28] using soft lithography method bonded to a glass slide. Photoresist KMPR 1025 (MicroChem) is used for the process. The continuous reservoir region of the mold is made by attaching a 22*22 mm cover glass No. 2 (Fisher Scientific) using Norland Optical Adhesive (NOA 81- Norland products Inc.) to the silicon-made portion of the channel. NOA is cured with UV for 5 seconds (400 Watt- DYMAX Corporation).

Device operation

For the experiments with Pico-Surf oil, channels are filled with Rain-x (water repellent) for 30 minutes and for the experiments with FC 40, 2 percent trichloro(1H,1H,2H,2H-perfluorooctyl)silane (Sigma Aldrich) in FC 40 is used. Then channels are rinsed with the appropriate oil for each experiment to create fluorinated surfaces. After filling the continuous-phase reservoir with oil using a syringe (no pump is needed), then the ferrofluid-containing fluid can be added to the inlet reservoir. Then the magnet is positioned at the bottom of the channel

and the distance of the magnet from the step is adjusted from 0 to 2500 μm downstream of the step (a line connecting the center of the ferrofluid reservoir to the center of the magnet passes through the middle of the connecting channel and is parallel to the channel walls to have a symmetric field). Fluid then is attracted toward the magnet driven only by the magnetic force and once it passes the step, droplets form. In figure 1 droplet generation by using only a small external magnet is shown.

Magnetic nanoparticles

In the experiments, two different aqueous ferrofluids were used: EMG 408 (ferrotec Co.) and concentrated Feraheme (ferumoxytol-amag pharmaceuticals), which consist of *10 nm* and *20 nm* magnetic nanoparticles respectively. Ferrofluid refers to a fluid that contains suspended magnetic nanoparticles that makes the bulk fluid susceptible to magnetic fields. The size of the magnetic particles should be small enough such that the magnetic particles do not sediment. In other words, the thermal energy is higher than the gravitational energy and the magnetic energy (because of an external magnet) that would otherwise tend to cause sedimentation of the particles[29]. Most of our experiments are done using EMG 408. Around 1.2 percent of the total fluid volume in EMG 408 is magnetic nanoparticles and the rest is water, surfactant is also used for stability. Saturation magnetization of the EMG 408 ferrofluid is 0.006 Tesla. For the experiments using devices containing multiple inlets and step we used concentrated ferumoxytol. *1 ml* of ferumoxytol was centrifuged for 3 hours at 14000 rpm and then the top 300 microliter was removed to make it more concentrated in order to be more susceptible to magnetic field. Magnetic nanoparticles in ferumoxytol are coated with polyglucose sorbitol carboxymethyl ether which is a sugar and makes it a good choice for applications where direct contact of other materials with iron could cause problems. Other ferrofluids or aqueous solutions with suspended

magnetic particles could also be employed, preferably ferrofluids that are aqueous-based and biocompatible should be employed to enable downstream assays.

Oils

The oils tested were both fluorinated low viscosity oils Pico-Surf 1 (2 percent and 5 percent in Novec 7500-Dolomite catalog numbers 3200211and 3200214) (*1.24 cP*) and FC 40 (*3.5 cP*) (Sigma Aldrich F9755). Surface tension of 0 percent surfactant oil (Novec 7500), 2 percent Pico-Surf, and FC 40 are *16.2, 7*, and *16 mN/m* respectively. In addition, the density of Novec and FC 40 are *1614* and 1850 kg/m^3.

Magnetic flux density gradient calculation

The magnet used is from K&J magnetics (D68). Comsol simulations were used to calculate the magnetic field in space, knowing the overall magnetic strength (supplementary figure 3) which was verified by comparing the results with experimental measurements of magnetic flux density using an FW Bell Series 9900 gaussmeter for different distances from the magnet. Magnetic fields module was used and Ampere's equation was solved (stationary study- no current) with a boundary condition of magnetic insulation (the magnet is modeled as a square- 0.4 T surface flux density). Then the magnetic flux density values (X-component) along the line connecting the center of the ferrofluid reservoir to the center of the magnet that also passes through the middle of the connecting channel and is parallel to the channel walls is exported as a function of distance from the magnet. Finally the slope at each point in the graph of the magnetic flux density as a function of distance from the magnet (supplementary figure 3B) yields the gradient of the flux density in that direction.

High-speed imaging and droplet generation rate calculation

High-speed images of the droplet formation process were recorded using a Phantom V710 at

1000 fps (Nikon eclipse Ti-U microscope (4x objective) is used). Each data point in figure 3 shows the average droplet generation rate which is equal to *100 droplets/ T(sec)* where *T* is the time required for generating 100 droplets for each condition.

Droplet formation process

In our system, the magnetic field alone acts to drive flow of ferrofluids and subsequently generate an emulsion at a junction with a step change in confinement. The microfluidic device consists of an inlet or ferrofluid reservoir, a continuous-phase reservoir, as well as terrace and connecting channels between the ferrofluid reservoir and the continuous-phase reservoir (figure 1). A step is formed at the interface between the microfluidic channel and the continuous-phase reservoir. The magnet is placed under the chip (after the step) and when the fluid, driven by the external magnet, reaches the step, it starts to pinch off and droplets are formed. The governing equations for the motion of the fluid inside the microchannel are Navier-Stokes equations with a magnetic gradient-based body force on the magnetic nanoparticles. This is assumed to be transduced to the surrounding fluid because of the small size and large number density of nanoparticles. It should be noted that the magnetic field used in the experiments is always greater than *0.01T* and this value is above the saturation magnetization of the nanoparticles (EMG 408), such that the body force on the ferrofluid is proportional to $m\boldsymbol{\nabla B}$, where *m* is the total magnetic moment per unit volume (proportional to number of nanoparticles) and **B** is the magnetic flux density[30].

Considering that in our method the flow rates are low (less than 0.2 $\mu l/\min$) and the Reynolds number $\frac{\rho V D_h}{\mu}$ (ρ is density of the fluid, V is the average fluid velocity, μ is fluid dynamic

viscosity and D_h is the hydraulic diameter) is less than 0.03, we can assume inertial forces are negligible. Hence the Navier-Stokes equations (considering Stokes flow) can be written as follows for the ferrofluid phase:

$$-\boldsymbol{\nabla} p + \mu_f \boldsymbol{\nabla}^2 \boldsymbol{u} + m\boldsymbol{\nabla B} = 0 \qquad (1)$$

$$\boldsymbol{\nabla}.\boldsymbol{u} = 0 \qquad (2)$$

p, $\boldsymbol{u}$ and μ_f are pressure, velocity (vector) and dynamic viscosity of the ferrofluid respectively. For the oil phase the equation of motion is similar to equation 1 but without the magnetic body force term.

Because of the interfacial tensions, a force is generated on the ferrofluid-oil interface which opposes expansion of the interface. For a constant surface tension over the boundary, the force on a small surface element *ds* is given by

$$\boldsymbol{n}\gamma(\boldsymbol{\nabla}.\boldsymbol{n})\ \mathrm{ds} = \boldsymbol{n}\gamma\ (\tfrac{1}{R_i} + \tfrac{1}{R_o})\ \mathrm{ds} \qquad (3)$$

where $\frac{1}{R_i}$ and $\frac{1}{R_o}$ specify in-plane and out-of-plane curvatures respectively, and γ is the interfacial tension on the interface. The normal vector to the interface is denoted by $\boldsymbol{n}$. Kinematic and velocity boundary conditions should also be considered for the evolution of the shape of the interface as a function of time as discussed in the work of Stone and Leal[31].

In the absence of pumps that apply a pressure gradient, equation 1 indicates that the magnetic

body force drives the flow.

A thorough understanding of the pinch off mechanism necessitates solving the governing equations of motion numerically for both oil and ferrofluid phase with appropriate boundary conditions imposed by walls and the interface. Numerical solutions can provide information about the time-dependent progress of the ferrofluid in the step and terrace geometry.

We also make some simplifying assumptions to provide an explanation of the pinch off mechanism that is consistent with our experimental results. In our method, the oil is quiescent and as figure 2A shows, first ferrofluid expands into the terrace region. Once the ferrofluid phase tip passes the step, where it can grow in the *Z* direction (figure 2B), the in-plane curvature in the terrace region *1/R* also starts to decrease and pinch off occurs (figure 2 A,C). It should be noted that this change in curvature (figure 2C) implies a change in pressure across the interface in the terrace region based on equation 3. The observed process is similar to the work of Dangla et al.[19] where they show the change in the curvature of the tip of the fluid in a geometry with a gradient of confinement causes a change in the curvature of the fluid boundary upstream leading to pinch-off for a slow droplet generation process *O(sec)*. However, here we have a sudden expansion instead of a gradient of confinement and this changes the timescale of the process *O(msec*). The similarity in the process suggests that the gradient in surface tension force plays a dominant role in generating a transient pressure jump according to equation 3, that leads to draining of fluid from the terrace region faster than it is refilled by the magnet-driven flow and once *1/R* becomes negative (figure 2C) pinch-off is initiated similar to a Rayleigh instability. Future numerical work will be useful to further test this mechanism. Faster flow due to increased width also

contributes to this process.

Controlling droplet generation rate

We observe that as fluid passes the step, pinch off occurs passively to create drops of a geometrically-determined size, such that the flow rate of the ferrofluid instead controls droplet generation rate. A simplified model for the fluid flow can be derived from equations (1-3), where we only consider Stokes flow in a rectangular channel of length L, W(Width)>>H(Height) and both inlet and outlet open to atmospheric pressure (figure 3B). In this case the pressure differences across the connecting channel (ΔP_{12}) in the direction of the flow goes to zero and consists of: (1) ΔP_f: The viscous pressure drop in the ferrofluid phase for a flow rate of Q and force per unit area due to the magnetic body force (2) ΔP_o: The viscous pressure drop in the oil phase for a flow rate of Q (3) ΔP_i: The pressure jump across the interface of ferrofluid and oil. Viscous pressure drop is reported in many works previously where a fluid fills a channel and is in contact with the wall[32,33]. ΔP_f is calculated with the assumption of having a thin stagnant film of oil (h) between the ferrofluid phase and the walls[34], and since the flow rate is low, the film thickness h is expected to be negligible. Based on equations 1,2 we derive ΔP_f considering the velocity in the channel varies only in the Z direction corresponding to the short channel height:

$$(-\boldsymbol{\nabla} p_f + m\boldsymbol{\nabla B})/\mu_f = -\boldsymbol{\nabla}^2 \boldsymbol{u} = -\partial^2 u/\partial z^2 \qquad (4)$$

We assume a constant magnetic field gradient over the channel length such that we can approximate ($\nabla B = \Delta B/L_1$). ∇B is the change in B (magnetic flux density) across the channel length. Thus:

$$u = \frac{\left(\frac{-\Delta P_f}{L_1} + \frac{m\Delta B}{L_1}\right)}{\mu_f} \iint dzdz \quad (5)$$

$$u = \left(\frac{-\Delta P_f + m\Delta B}{2\mu_f L_1}\right)(z^2 + c_1 z + c_2) \quad (6)$$

Constants c_1 and c_2 are calculated using no-slip boundary condition at *z=0, H-h*. The flow rate then is calculated as follows:

$$Q=(W-h) \int_0^{H-h} u dz \quad (7)$$

By substituting equation 6 into equation 7 and considering no-slip boundary conditions we arrive at:

$$\Delta P_f = -\frac{12\mu_f L_1 Q}{(W-h)(H-h)^3} + m\Delta B \quad (8)$$

where μ_f is the viscosity of the ferrofluid. ΔP_0 is calculated in a similar manner to equation 8 considering the viscosity of the oil μ_o without the magnetic forcing term and the film thickness h. ΔP_i, as equation (3) shows, is proportional to interfacial tension and curvatures. Bretherton[35] showed that the pressure jump across an interface and the thickness of the lubrication layer, h, is proportional to the velocity of the fluid as well as the surface tension forces. This analysis was found to be valid when considering a dispersed phase viscosity that is negligible compared to that of the continuous phase. However there has not been any equation developed that considers

the effect of viscosity of the dispersed phase completely. Here we use $c\gamma$ in a simplified form for ΔP_i where c is determined by channel dimensions and fluid velocity and γ is interfacial tension. Thus the total pressure variation from the inlet to the end of the connecting channel is calculated as follows:

$$\Delta P_{12} = \Delta P_f + \Delta P_o + \Delta P_i \quad (9)$$

$$0 = -\frac{12\mu_f L_1 Q}{(W-h)(H-h)^3} + m\Delta B - \frac{12\mu_o L_2 Q}{(W)(H)^3} - c\gamma \quad (10)$$

$$Q = \frac{m\Delta B - c\gamma}{\frac{12\mu_f L_1}{(W-h)(H-h)^3} + \frac{12\mu_o L_2}{(W)(H)^3}} \quad (11)$$

As shown in equation 11 and figure 3B, Q (volumetric flow rate) is proportional to the magnetic body force and opposing forces are the interfacial and viscous forces.

By increasing the driving force (magnetic force) or decreasing forces opposing expansion of the interface (interfacial and viscous forces) the fluid is expected to reach a higher average velocity, which results in a higher droplet generation rate (since the volume of each droplet is controlled by the terrace dimensions and is independent of flow rate). In fact, droplet generation rate increases as a function of increasing magnetic force and decreasing surface tension (figure 3A, equation 11). By adjusting the position of the magnet to create a higher magnetic field gradient (supplementary figure 3), droplet generation rate increases linearly (figure 3A). In addition, increasing surfactant (0 to 5 percent pico surf in Novec 7500) reduces the surface tension force

(equation 11) and droplet generation rate increases (figure 3A).

The driving force also increased with the addition of more magnetic nanoparticles to the solution (increasing the magnetic moment density in equation 11) also resulting in a higher droplet generation rate (figure 3C).

We observed an increase in the slope of droplet generation rate as a function of the volume fraction of magnetic nanoparticles above volume fractions of 0.005. Below 0.005 we observed that immediately following pinch-off fluid starts re-filling from a location more upstream in the connecting-channel region (highly confined in all directions), however at higher volume fractions re-filling initiates in the terrace which is not confined in the *Y* direction and is closer to the driving magnet. It should be noted that surface tension also slightly increases by increasing the number of nanoparticles (around 5 percent)[36] (surface tension of EMG 408 (1 percent volume fraction) is *60 mN/m*), however magnetic body force changes significantly more over the range tested.

Viscosity of the oil also plays an important role in the rate of droplet formation, and as the results in figure 3D show, by decreasing the viscosity (1.24 cP (Novec 7500) instead of 3.5 cP (FC 40)) fluidic resistance decreases and droplet generation increases (surface tension of Novec 7500 and FC 40 are 16.2 and 16 *mN/m* respectively).

The maximum droplet generation rate we were able to achieve with a cylindrical magnet (K&J magnetics-D68), is about 80 droplets per second per connecting channel for 5 percent pico-surf oil using EMG 408 ferrofluid. Consequently, a 10 μl solution would be emulsified to 85 μm

droplets in less than 10 minutes with the setup shown in figure 1, which consists of 10 parallelized connecting channels.

Finally, we also examined breakup with a pressure driven flow (replacing the magnetic body force in equation 1). Capillary number $Ca=\mu V/\gamma$ is the ratio of viscous forces to surface tension, where μ is the dynamic viscosity of the fluid, V is a characteristic velocity and γ is the surface tension. Surface tension forces are dominant compared to viscous forces in our system where $Ca < 0.01$. At low flow rates (less than 1 $\mu l/min$, $Ca < 0.05$) droplet formation was observed; However, at higher flow rates (higher than 2 $\mu l/min$, $Ca > 0.1$), where viscous stresses play a significant role compared to surface tension forces, as is shown in supplementary figure 1 droplets did not form and fluid expanded into the reservoir. This shows that there is a maximum droplet generation rate specific to each geometry in this system even when there is no pump involved.

The terrace length determines the amount of fluid that accumulates prior to pinch-off and controls drop size. Droplet pinch-off is observed to initiate at the beginning of the terrace region for all cases, thus larger droplets are expected for longer terrace regions since the volume of the fluid downstream of the breakup point is greater. In fact, we observed an increase in diameter from 85 μm to 125 μm by increasing the terrace length from 60 to 90 μm (figure 1D). It should be noted that even without the terrace droplets still form (supplementary figure 2) and the same mechanism is observed at the step junction. One of the important features of this technique is that the final droplet size is not dependent on the properties of the fluids for the ranges of surface tension, viscosities and magnetic forces tested in the low capillary number regime.

On-chip emulsification and mixing

Removing pumps does not limit the ability of this technique to perform more complex on-chip operations. One of the important features required for droplet or digital microfluidics is the ability to mix reagents on chip and form compartmentalized drops afterwards. This is critical for some analytical approaches that rely on molecular chain reactions, because if the reactive reagents are mixed in a one-inlet device, chain reactions can initiate as soon as the mixing occurs. Therefore, all droplets will contain products of the reaction such that concentration-dependent detection of the target in the droplets is not possible[37].

In order to show efficient mixing of reagents, a two-inlet device (with a step) shown in figure 4 is used. The device is similar to the device shown in figure 1 with a step change in height, but with 2 separate inlets. The magnet is positioned at the middle (50 μm downstream of the step) to have an equal magnetic body force on both solutions, attracting them toward the step. From one inlet, 14 μl concentrated ferumoxytol mixed with 1 μl DI water was used. On the other hand, 14 μl concentrated ferumoxytol mixed with 1 μl fluorescein was introduced to the other inlet. As fluorescent images in figure 4A show, solutions mix efficiently and half of the connecting channel is filled with each solution when droplets are formed. In addition, we demonstrated a 3-inlet device with a step downstream (figure 4B) where the middle inlet contains fluorescein and the other two inlets contain DI water instead of fluorescein. Mixing of reagents occurs inside the droplets because of internal flows in droplets[38] and the presence of magnetic nanoparticles. A histogram of fluorescent intensity describing the distribution in droplets formed with the 2-inlet device indicate stable mixing using the approach (figure 4C).

Conclusion

In this work, we report a new mechanism for microfluidic droplet formation for fluids containing magnetic nanoparticles in a step emulsification device without any pumps driven solely by magnetic force. The ability to controllably form droplets without pumps could be beneficial for a variety of applications such as point-of-care assays and cell sorting in droplets. Droplet size is insensitive to flow rates, magnetic force and interfacial forces. Instead it is dominated by dimensions of the channel. On- chip mixing of different fluids and emulsifying them is easily achieved in this method in a step emulsification device with multiple inlets by only a small external magnet. Generated magnetic droplets could also be moved and manipulated by a magnet in the reservoir for different downstream applications[39].

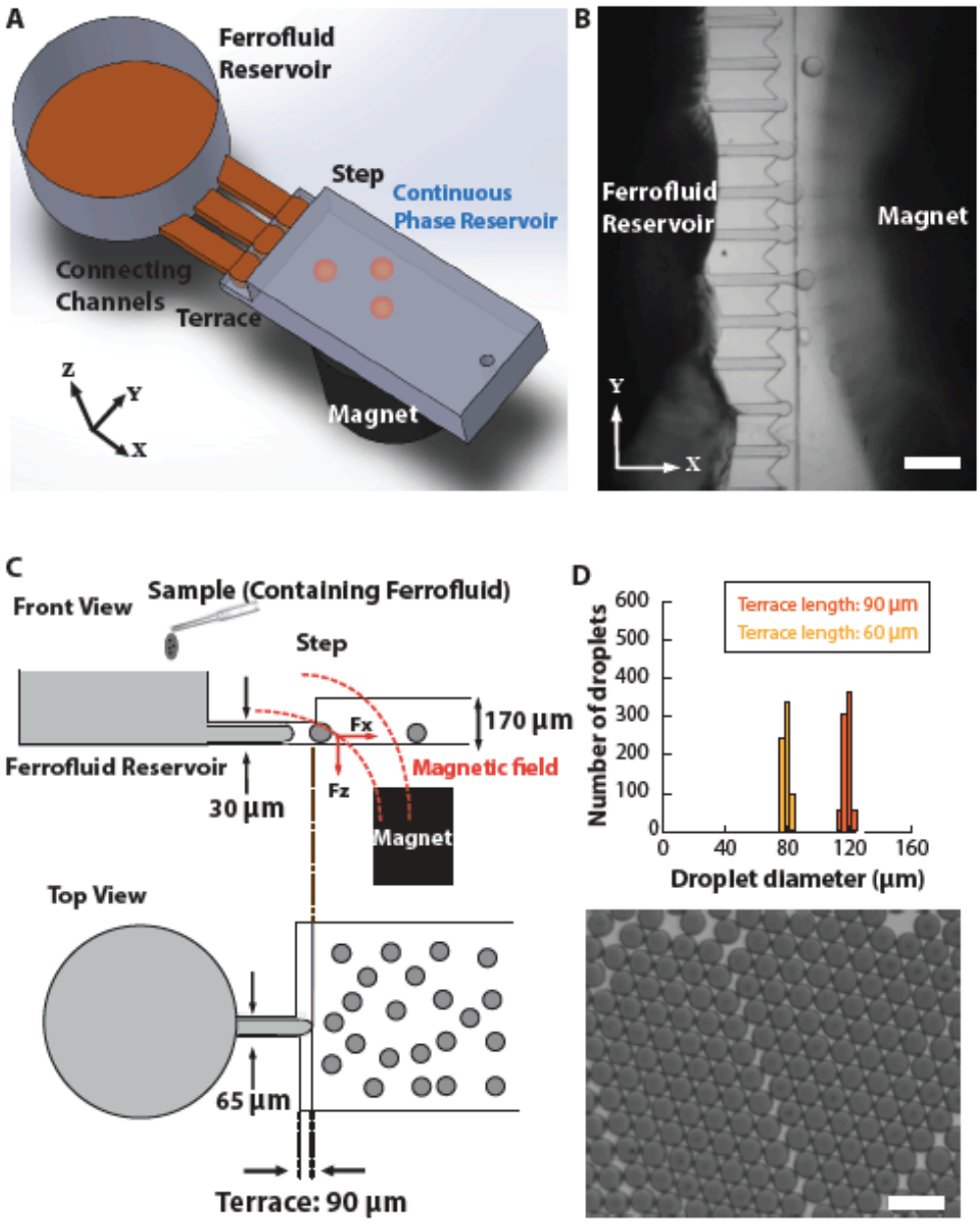

Figure 1: Schematic view of the magnetically driven microfluidic droplet generation technique using ferrofluids (without any external pumps). A) 3D view of the device consisting of a sample (containing ferrofluid) reservoir, connecting channels, terrace, step, continuous phase reservoir, and magnet. B) Experimental snapshot of high throughput droplet generation. C) Front view and top view of the device displaying dimensions of each part of the channel. D) Formed magnetic droplets with a uniform size distribution. Scale bar in all images is 250mm.

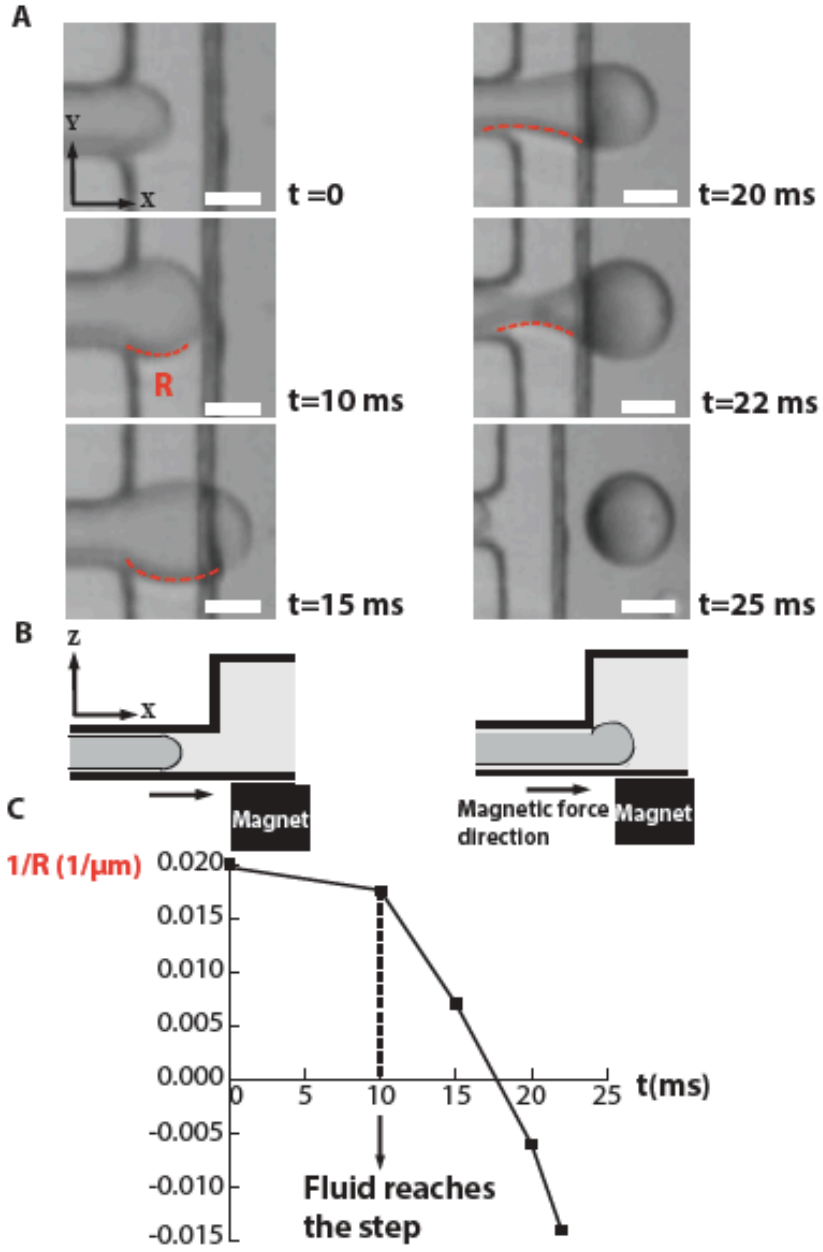

Figure 2: Droplet generation process: A) Magnetic fluid is attracted toward the step because of the gradient in magnetic field. As the fluid passes the step, the tip starts to grow in the Z direction and in-plane curvature at the terrace also starts to change leading to the eventual pinch-off.

B) Cross section of the channel in XZ before and after the fluid reaches the step.

C) 1/R as a function of time during the droplet generation process

(continuous phase is 2 percent Pico-Surf and the magnetic flux density

gradient is 0.07 Tesla/mm). Scale bar in all images is 50mm.

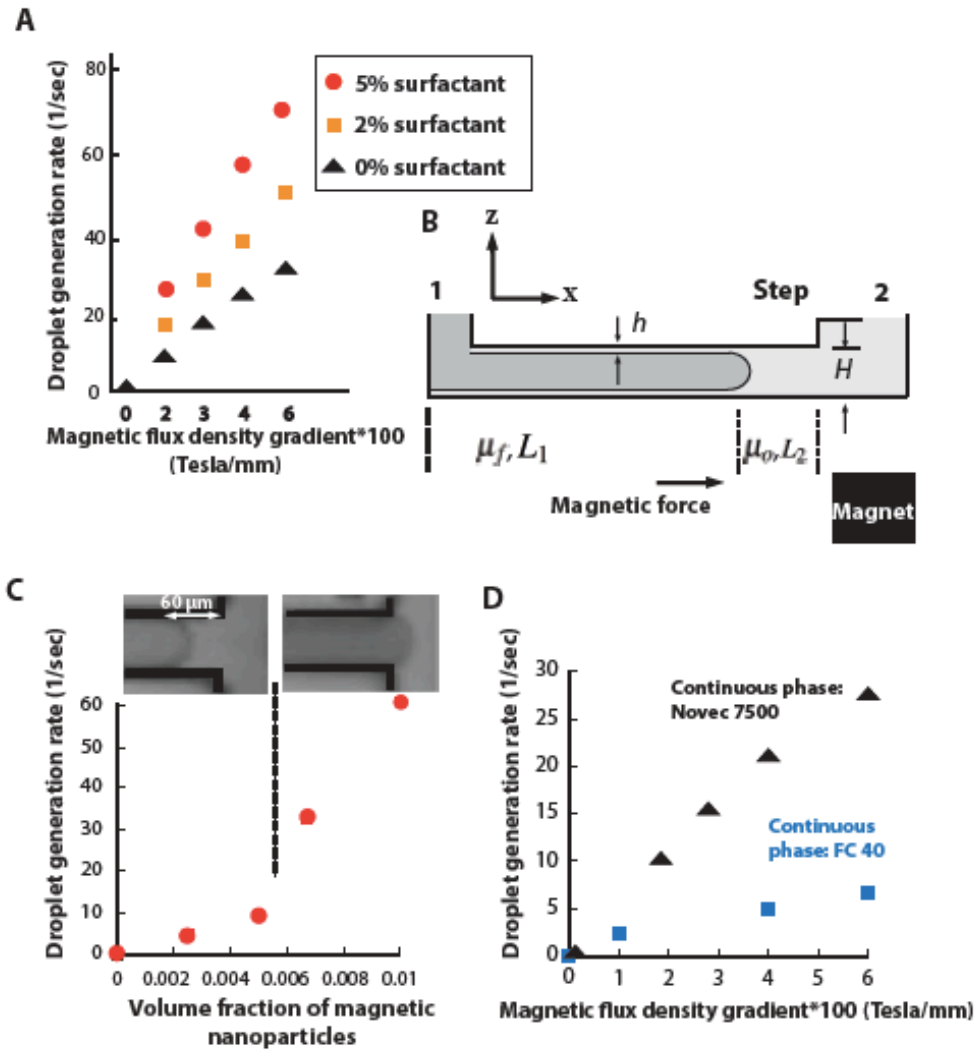

Figure 3: A) Average droplet generation rate as a function of gradient of magnetic flux density and surface tension. B) Schematic view of the simplified model used. Average droplet generation rate as a function of C) volume fraction of magnetic nanoparticles, D) viscosity of the oil.

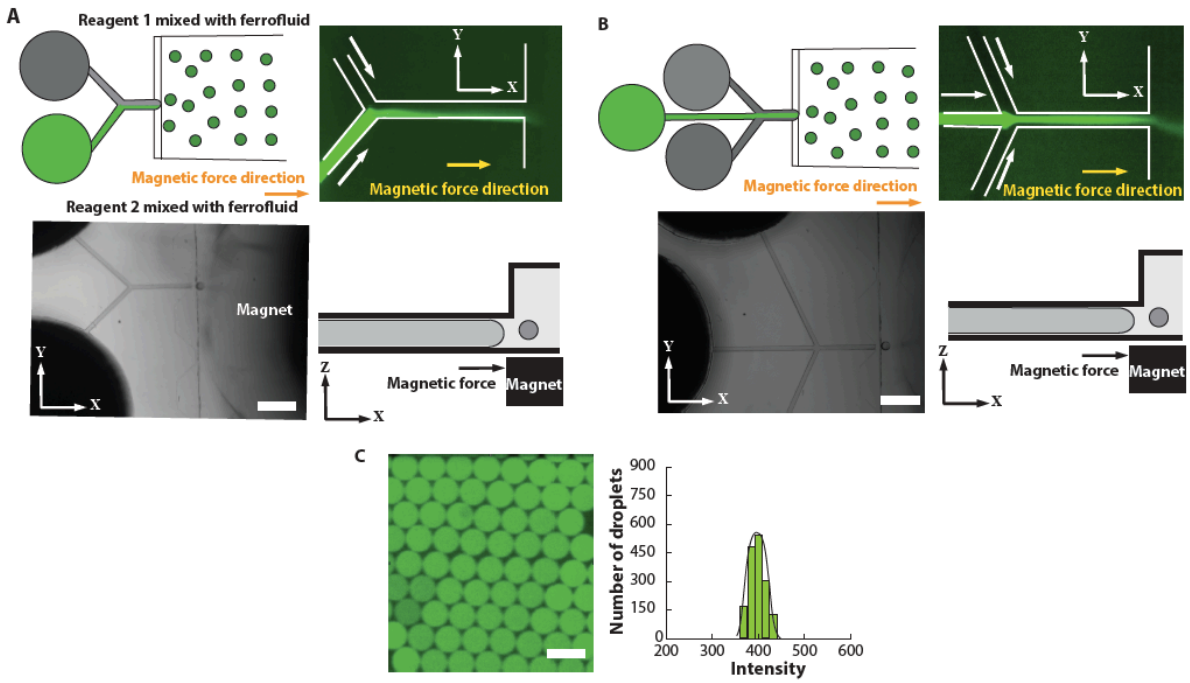

Figure 4: On-chip mixing and emulsification using only an external magnet. A) Mixing fluids in a two inlet device (similar to the step emulsification device shown in figure 1 but with 2 separate inlets (ferrofluid reservoirs)) (fluid in the bottom inlet contains fluorescein in addition to magnetic nanoparticles. Scale bar is 400mm. B) Mixing fluids in a three inlet device (fluid in the middle inlet contains fluorescein in addition to magnetic nanoparticles). Scale bar is 400mm. C) Histogram showing uniform signal intensities of the formed droplets (2 inlet device). Reported intensity for each droplet is the average of the intensities of the 100 pixels around the center of that droplet. The exposure time is 1 second. Scale bar is 200mm.

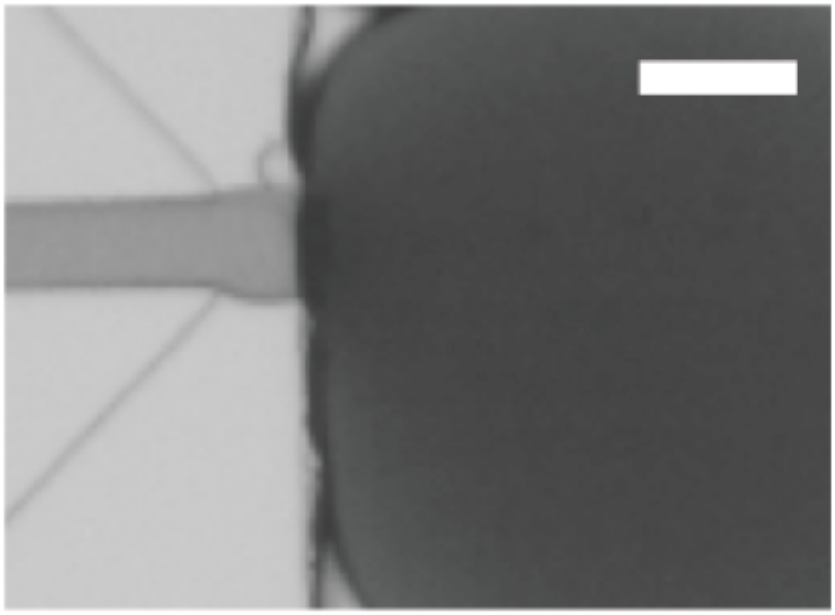

Supplementary figure 1: High flow rate leads to jetting and no drop formation in the step junction. A test with a syringe pump at 2μl/min (no magnet- Capillary number>0.1. Scale bar is 80 μm)

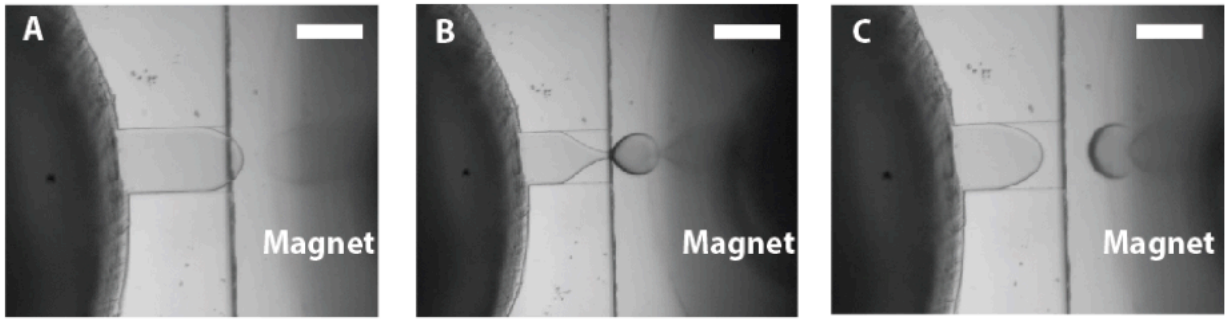

Supplementary figure 2: Droplet generation without the terrace region. (Pinch-off of the drop occurs within the channel adjoining the reservoir. Scale bar is 150 μm). A: 0, B: 35 ms, C: 60 ms.

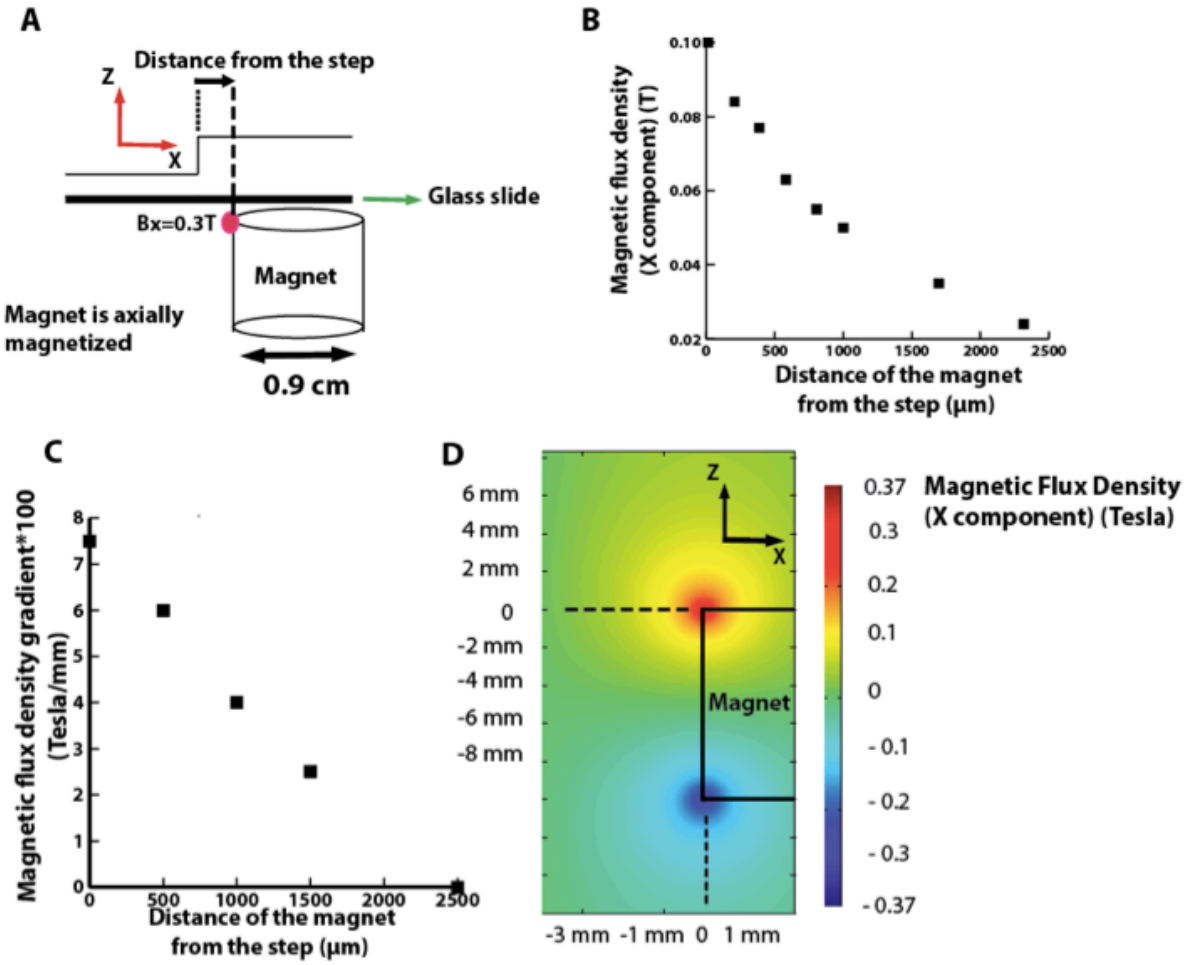

Supplementary figure 3: Magnet location and characterization of the magnetic flux density based on 2D comsol simulation. Magnet corner (top left) is located at (0, 0). A) Magnet location and size. B) Magnetic flux density in X direction and C) Magnetic flux density gradient in the X direction that are calculated based on D) comsol simulation.

References:

1 E.Z. Macosko, et al., Cell, 2015, 161(5), 1202-1214

2 V. Srinivasan, V.K. Pamula, and R.B. Fair, Lab. Chip, 2004, 4(4), 310-315.

3 M.T. Guo, A. Rotem, J.A. Heyman, and D.A. Weitz, Lab. Chip, 2012, 12(12), 2146-2155.

4 S.Y. Teh, R. Lin, L.H. Hung, and A.P. Lee, Lab. Chip, 2008, 8(2), 198-220.

5 I. Barbulovic-Nad, H. Yang, P.S. Park, and A.R. Wheeler, Lab. Chip, 2008, 8(4), 519-526.

6 S.M. Fix, M.A. Borden, and P.A. Dayton, J. Control. Release, 2015, 209, 139-149.

7 D.R. Griffin, W.M. Weaver, P.O. Scumpia, D. Di Carlo, and T. Segura, Nat. Mater., 2015, 14(7), 737-744.

8 J.F. Edd, et al., Lab. Chip, 2008, 8(8), 1262-1264.

9 S. Kahkeshani, H. Haddadi, and D. Di Carlo, J. Fluid Mech., 2016, 786, R3.

10 S.L. Anna, N. Bontoux, and H.A. Stone, Appl. Phys. Lett., 2003, 82(3), 364-366.

11 A.S. Utada et al., Science, 2005, 308(5721), 537-541.

12 T. Thorsen, R.W. Roberts, F.H. Arnold, and S.R. Quake, Phys. Rev. Lett., 2001, 86(18), 4163.

13 P. Garstecki, M.J. Fuerstman, H.A. Stone, and G.M. Whitesides, Lab. Chip, 2006, 6(3), 437-446.

14 V. Van Steijn, C.R. Kleijn, and M.T. Kreutzer, Phys. Rev. Lett., 2009, 103(21), 214501.

15 S. Sugiura, M. Nakajima, and M. Seki, Langmuir, 2002, 18(10), 3854-3859.

16 Z. Li, A.M. Leshansky, L.M. Pismen, and P. Tabeling, Lab. Chip, 2015, 15(4), 1023-1031.

17 M. Hein, J.B. Fleury, and R. Seemann, Soft Matter, 2015, 11(26), 5246-5252.

18 N. Mittal, C. Cohen, J. Bibette, and N. Bremond, Phys. Fluids, 2014, 26(8), 082109.

19 R. Dangla, S.C. Kayi, and C.N. Baroud, Proc. of Nat. Acad. Sci., 2013, 110(3), 853-858.

20 F. Schuler, F. Schwemmer, M. Trotter, S.Wadle, R. Zengerle, F. von Stetten and N. Paust, Lab. Chip, 2015, 15(13), 2759-2766.

21 F. Schuler, et al., Lab. Chip, 2016, 16(1), 208-216.

22 N. Pamme, Lab. Chip, 2006, 6(1), 24-38.

23 J. Liu, S.H. Tan, Y.F. YAP, M.Y. Ng, and N.T. Nguyen, Microfluid. Nanofluid., 2011, 11(2), 177-187.

24 Z.Z. Chong, S.H. Tan, A.M. Gañán-Calvo, S.B. Tor, N.H. Loh, and N.T. Nguyen, Lab. Chip, 2016, 16(1), 35-58.

25 Y. Wu, T.Fu, Y.Ma, and H.Z. Li, Microfluid. Nanofluid., 2015,
18(1), 19-27.

26 J. Liu, Y.F. Yap, and N.T. Nguyen, Phys. Fluids, 2011, 23(7), 072008.

27 S.H. Tan, N.T. Nguyen, L. Yobas, and T.G. Kang, J. Micromech. Microeng., 2010, 20(4), 045004.

28 D.C. Duffy, J.C. McDonald, O.J. Schueller, and G.M. Whitesides, Anal. Chem., 1998, 70(23), 4974-4984.

29 R.E. Rosensweig, 2013, Ferrohydrodynamics, Courier Corporation.

30 D.W. Inglis, R. Riehn, J.C. Sturm, and R.H. Austin, Appl. Phys. Lett., 2006, 99(8), 08K101.

31 H.A. Stone and L.G. Leal, J. Fluid. Mech., 1989, 198, 399-427.

32 F. M. White, Viscous Fluid Flow, McGraw-Hill Companies, Inc, Boston, 2006.

33 K. Hattori, S. Sugiura, and T. Kanamori, Lab. Chip, 2009, 9(12), 1763-1772.

34 J. Jovanovic, et al., Chem. Eng. Sci., 2011, 66(1), 42-54.

35 F.P. Bretherton, J. Fluid. Mech., 1961, 10(2), 166-188.

36 M.S. Dababneh, N.Y. Ayoub, I. Odeh, and N.M. Laham, J. Magn. Magn. Mater., 1993,

125(1), 34-38.

37 M. Baker, Nat. Methods, 2012, 9(6), 541.

38 C.N. Baroud, F. Gallaire, and R. Dangla, Lab. Chip, 2010, 10(16), 2032-2045.

39 G. Katsikis, J.S. Cybulski, and M. Prakash, Nature Physics, 2015.

Chapter 4

Magnetic droplet dosing device for point-of-care quantification of biomolecules

ABSTRACT: Here we present a nanoliter sample release platform using a magnet for point-of-care generation of a specific number of droplets (dosing) and delivery of nanoliter-dosages of sample to the reaction mixture wells (reagents), which after amplification could reveal an estimation of the number of target DNA molecules in the original sample. The device could be used in limited-resource settings since it only requires a magnet for nanoliter dispensing of the sample (pre-mixed with coated magnetic nanoparticles) and batteries for the imaging system. Number of generated droplets could be controlled using the time that the magnetic field is applied, enabling sample dosages in the pico- or nanoliter ranges. Thus, the platform could be used for low-volume samples and multiplexed assays for detection of biomolecules using nanoliters of sample for each assay. Here we demonstrate detection of lambda DNA molecules at different concentrations as a proof of concept using loop-mediated isothermal DNA amplification (LAMP). This platform can be applied to a number of different samples after the addition of magnetic nanoparticles to allow for magnetically-driven digital (droplet) point-of-care diagnostics.

Digital (droplet) point of care diagnostics is a rapidly growing field enabled by automated and accurate sample preparation and manipulation at nano and micro scale[1-6]. Using droplet microfluidics, target biomolecules could be isolated, amplified and detected at dilute concentrations. However, most of the developed technologies require operation in the lab and cannot be used in limited resource settings. Translating digital (droplet) diagnostic technologies for point of care applications requires sample preparation[7] techniques that do not require the use of complicated systems, droplet generation techniques which do not depend on electricity or expensive equipment, precise temperature control for assay reactions, having a wide dynamic range for droplet release, ability to perform multiple assays on a low volume sample, and a portable imaging system that could be assembled from available platforms such as cell phones[6, 8-10] for readout and transfer of data[11-13] while managing to reduce movements of droplets. Challenges in all of the mentioned areas have hindered commercialization of the digital point of care systems[14].

Few commercial products are addressing these challenges with different techniques. Advanced Liquid Logic company has developed one of the few commercially available point of care droplet diagnostic devices, which uses an electrowetting-based digital microfluidic platform to control droplet motion[1]. The system is complex due to the precision required for controlling motion of droplets and electro-chemical sensors are designed for the readout.

The SlipChip, another product developed to overcome some of the challenges associated with droplets, allows for reagent mixing by mechanically moving wells and merging the sample wells

and reagent wells. Therefore, instead of droplets, nanoliter wells have been used for sample and reagents separately and then they are merged. Based on the number and size of the wells that generate amplified signal, concentration of target molecules are estimated. The number and size of the wells depends on the initial design and it could not be changed during the process. Furthermore, Kahkeshani and Di Carlo[2] have shown a drop formation technique using only an external magnet in a step emulsification geometry that is suitable for point of care devices when sample is mixed with magnetic nanoparticles (ferrofluids) and precise on-demand dosing of the sample is achieved by an external magnet.

Here we show a system that addresses the mentioned challenges by removing pumps, and a droplet delivery system that removes the need for controlling movement of droplets during imaging. This system is able to deliver different dosages of nanoliter droplets to 100 microliter reaction mixture wells using a small permanent magnet and image using a mobile phone reader. The target molecule concentration can be determined by comparing fluorescent signal presence in wells where various sample volumes were introduced. One of the main advantages of this system is that instead of using microliters of a sample for quantification of the target molecule, it uses nanoliters of sample, allowing for multiplexing with low sample volumes. If instead of pipetting microliters of sample in each step, pico- or nanoliters of sample are used for amplification and detection steps, hundreds of different assays could be tested on 1 μL of sample. Especially for point-of-care platforms, there is a need for a self-contained system where contamination is avoided and many different assays could be tested on a sample[17,18]. The other advantage of the system is amplification occurs in cm-size wells, which removes the need for

controlling droplet motion, while still maintaining nanoliter-level sample volume, enabling the use of hand-held imaging systems[8].

Droplet dosing device mechanism

The platform is shown in figure 1 and the process is done in 4 steps. We demonstrate the use of this platform using loop-mediated isothermal DNA amplification (LAMP) [19, 20] with the addition of hydroxynaphthol blue (HNB) [21], demonstrated recently[22] to be useful for point of care applications due to higher signal to noise ratio and also high stability over thermal fluctuations over time[11]. Each reaction mixture well is filled with 100 µl of the assay components, as it is detailed in the methods section, and the lambda DNA sample mixed with magnetic nanoparticles is added magnetically in different nanoliter dosages to each well to quantify the DNA sample concentration, as it will be discussed. It should be noted that this approach is different than "digital LAMP" [23-27] where after emulsification of the whole sample, number of amplified droplets is counted.

Mechanism of droplet formation in this system is shown in our previous work[2]. Magnetic nanoparticles are mixed with the sample so that the sample would be susceptible to magnetic field and attracted toward the magnet and emulsified in a step emulsification geometry, where sudden change in Laplace pressure due to increase of radius of curvature at the step causes a change in pressure and curvature of the fluid upstream in terrace region. The droplet generation frequency could be adjusted by the strength of the magnetic field, concentration of the magnetic nanoparticles in the solution, viscosity and/or surface tension of the oil or the sample solution as shown in the work of Kahkeshani and Di Carlo. In this system final droplet size is dependent on

channel geometry for the low capillary number regime, which makes it very robust for precise dosing in point of care settings.

Four reaction mixture wells are used for four different dosages. Number of reaction mixture wells is adjustable. At least 3 reaction wells are required, and increasing number of reaction mixture wells and corresponding dosages would achieve more accurate diagnosis. The other components of the device consist of the sample reservoir, oil reservoir, step and connecting channel between sample reservoir and the oil reservoir.

After emulsifying desired dosage (step 1), delivery is achieved by placing a magnet on top of a reaction mixture well, which merges the sample with the other assay components for amplification (step 2). Then the process is repeated and another dosage of sample droplets is delivered to the second well. This continues until different dosages are delivered to the remaining wells. The dosages tested were 0 drops (control), 10 drops (10 nl), 40 drops (40 nl) and 100 drops (100 nl). In this platform, the assay dynamic range could be in the range of thousands, by adjusting the activation time of the magnet, 1-1000s of droplets could be released into each well and depending on the size of the droplets, released sample could be in the range of pico- to microliter. Once all the dosages are delivered to the designated wells and merged with the assay components, isothermal amplification is performed at 65 Celsius for 75 minutes (step 3) and then imaged using a mobile phone imaging system, bright wells could be detected and based on the number of drops that were initially delivered to those wells, concentration of DNA in the original sample is estimated (step 4). As shown in step 4 if all the wells except control are amplified, it means that the concentration of the DNA in the original sample is high and even in 10 nanoliter

of the sample DNA is detectable. However if only 40 nl and 100 nl wells are amplified (10 nl well is not amplified), then concentration of the DNA is lower compared to the previous case and it could be estimated around 2-4 copies per 40 nl. Finally, if only 100 nl well is amplified, this means that the sample has very low concentration of DNA (around 2-4 copies per 100 nl).

Here due to precision in the number of generated drops, and the ability to merging them with large volumes of reagents, estimation of number of target molecules could be done considering these benefits: using much lower sample volume for assay and since the sample is not mixed with reagents then it could be easily used for multiplexing for different assays simultaneously, simpler imaging system is needed since the droplets will not be imaged and the large reaction wells will be imaged, and temperature control over the reaction mixture wells is easier rather than control over individual droplets. Details of imaging system are discussed in methods section.

Results and discussion

In this study, magnetic nanoparticles were mixed with the target DNA sample using a pipette. However, magnetic sample mixing is possible for the generation of an automated point of care diagnostic system. Mixing at microscale at low Reynolds number flows is challenging due to laminar flow[28]. However, as shown in figure 2, using a small external magnet, mixing can be performed by moving the magnet back and forth in different directions. In order to show the efficiency of the mixing using this technique, we use a square microchannel with height of 150

μm. The device is filled with water first and then the ferrofluid containing magnetic nanoparticles is introduced. As shown in figure 2A, without the magnet after 30 minutes, ferrofluid remains at the inlet and diffusion occurs very slowly. To initiate the magnetic mixing we first place the magnet at the center of the channel, thus the magnetic nano particles and ferrofluid are attracted toward the magnet and they occupy the center region of the channel (figure 2B). If we remove the magnet, again only the slow diffusion of the nanoparticles would be the only contributing factor to the mixing of the two phases, however by starting moving magnet back and forth (cycles), collective effect of movement of magnetic nanoparticles due to magnetic field, displacement of the water phase due to the movement of the magnetic phase, and increased collision of nanoparticles which leads to enhanced diffusion of nanoparticles in water phase[29], the mixing of the both phases occurs (figure 2C,D). Following equations are governing equations of motion of ferrofluid phase and the magnetic force is accounted for as a body force due to presence of nanoparticles:

$$\rho_f \left(\frac{\partial \boldsymbol{u}}{\partial t} + \boldsymbol{u}.\boldsymbol{\nabla}\boldsymbol{u}\right) = -\boldsymbol{\nabla}p + \mu_f \boldsymbol{\nabla}^2\boldsymbol{u} + \boldsymbol{\nabla}(\boldsymbol{m}.\boldsymbol{B})$$

$$\boldsymbol{\nabla}.\boldsymbol{u} = 0, \quad \boldsymbol{\nabla}.\boldsymbol{B} = 0$$

where u is velocity, p is pressure, μ_f is the viscosity of the ferrofluid phase, ρ_f is the density of the ferrofluid phase, m is the magnetic moment and B is the magnetic flux density. To quantify the mixing efficiency, we use the mixing efficiency parameter used previously[28], defined as $1 - cv/cv_{max}$, where cv is the coefficient of variation of the signal intensity after mixing process is completed and cv_{max} is the coefficient of variation before mixing. When cv approaches 0 and intensity across the device becomes more uniform, the efficiency approaches the ideal case of 1. Figure 2E shows the summary of the mixing efficiency results for different

types of magnetic motions for different cycles. As shown, in under a minute, 85 percent efficiency is achieved.

After ferrofluid-sample mixing, the controllable nanoliter dosing begins. Controlled emulsification/release and high dynamic range are two important aspects of this device that is valuable for point of care applications. The average droplet generation rate is 4 droplets per second (4 nl/sec), and the number of generated droplets can be easily adjusted. The droplet size, as we have previously shown, is dependent on channel geometry. By decreasing of the length of the terrace region or connecting channel, smaller droplets can be generated. This ultimately results in a lower limit of sample dosing in the range of hundreds of picoliters. The upper limit, as shown in figure 3, is dependent on the interval that the magnet is activated. This could lead to a dynamic range around 1000s (number of droplets that could be generated at each step). Figure 3 shows the accurate nanoliter dosing for different actuation time using permanent magnet. The standard deviation for each time point is less than 10 percent, and the discrepancy is most likely due to the manual nature of placing and removing a magnet that could be resolved using an accurate electromagnet. We use 10 droplets (10nl), 40 droplets (40 nl), and 100 droplets (100 nl) and the variation in the number of generated droplets is around 1, 3, and 7 droplets, respectively.

Magnetic field required for forcing generated droplets to move from oil phase to the reaction mixture phase is about 0.1 Tesla,meaning the distance of the cylindrical magnet we used from the interface should be less than 1.5 cm. Once the droplets move to the reaction mixture phase, they

start merging with the mixture because both droplets and the mixture are aqueous based solutions. It should be noted that since the solution will be placed in 65 Celsius for 75 minutes afterwards, due to the thermal motion of the nanoparticles at that temperature, the mixing would be enhanced in that process.

Before imaging using cell phone, the best time point for the end-point measurement of the intensities should be determined. In order to do that, we have tested different cases with plate reader (Biotek Cytation 5) that we used to measure the fluorescence intensity during amplification in 5 minute intervals (figure 4). After delivering different dosages to different wells, the reaction mixtures (now also containing sample dosages) were collected using pipette and transferred to a well plate. Then the well plate is placed in the plate reader and the amplification and intensity measurements are done as is shown in figure 4.

Three different concentrations of the lambda DNA in the original sample are tested (figure 4): (A) 5.7E3 copies/µl, (B) 5.7E1 copies/µl, and (C) 5.7 copies/µl. For each concentration, 100 drops (100 nl), 40 drops (40 nl), and 10 drops (10 nl) of the sample are delivered magnetically to the reaction wells, and then collected and injected to wells of a well plate. The corresponding number of DNA molecules delivered in each case is also calculated based on the concentration of the DNA in the sample and the total volume of the generated droplets for each dosage and it is reported in the graphs (figure 4). Error bars, which are calculated based on the three separate experiments that has been done for each case (showing minimum and maximum), are shown only for the last data points to keep visibility of the data points. The error bar is less than 15

percent for all data points. For a sample containing 5.7E3 copies/µl of target DNA (shown in figure 4A) amplified fluorescence signal above background is detected after 55 minutes and reaches its maximum after 95 minutes. The control sample which does not have any sample, can generate signal after a long amplification time, similar to PCR, which could be related to contamination or other factors as reported in the work of Kong et al.[22] and is considered to be a false positive. Balancing assay time and limiting nonspecific amplification, a 75 minute endpoint was chosen for mobile phone measurement. The chosen endpoint was verified by testing lower DNA concentrations. Figure 4B shows the result for concentration 5.7E1 copies/µl. For 100 nl case, corresponding to about 6-7 copies, signal amplification is measurable after 55 minutes. However, for 40 nl, corresponding to 2-3 copies, almost half of the times the signal gets amplified by 55 minutes and half of the time it is similar to the control case shown in figure 4A. Thus, the limit of detection to determine the concentration accurately using nanoliter droplet delivery is about 5.7E1 copies/µl. Figure 4C shows the results for concentration 5.7 copies/µl, and the signal never gets amplified at 55 minutes due to extremely low number of DNA molecules. Considering results of all the concentrations, if the device is put in oven for 75 minutes and imaged after that using cell phone, the signal intensities of different wells could determine the concentration of DNA in the sample. Limit of detection depends on the type assay used.

After 75 minutes was determined as the endpoint for mobile phone imaging, the experiments conducted previously are repeated, and imaged directly on the device, instead of using a pipette to transfer the reaction solutions to a well plate for plate reader imaging. After dosing, the device

is placed in a 65 °C oven and the signal intensities are measured after 75 minutes. Other thermal control systems such as phase-change materials could be used for low-resource settings[30, 31]. The cell phone fluorescent imaging system is described in detail in the methods section. Figure 5A shows a selected snapshot of cell phone image for different delivered dosages of a specific concentration of DNA samples. Figure 5B shows corresponding fluorescent intensities of each well shown in figure 5A. Estimated DNA copies released in the reaction mixture wells are calculated based on the original DNA concentration and total volume of released droplets for each dosage, assuming sample homogeneity. It should be noted that the actual number of DNA copies delivered to each well might be slightly different than the reported estimated numbers, however it is not feasible to count the exact number of copies before the start of the amplification process. Based on the estimated values, summary of the all the intensities of different experiments is reported in figure 5C. As it is shown, for the wells where DNA amplification occurs due to presence of DNA, signal is around 60 and for negative wells signal is around 20. As the results show, if more than 2-3 copies are present at a reaction mixture well, this platform can detect it.

Conclusions

We present a platform that uses only a small external magnet for controllable emulsification (dosing) and delivery of the certain volume of the sample to different reaction wells prefilled with assay components, which after amplification and detection of bright (fluorescent) wells using cell phone could reveal number of target molecules in the sample. By using only nanoliters of sample at each step, this platform could be suitable for multiplexed assays for quantification

of different biomolecules. In order to be able to make this platform completely suitable for point of care usage, reagents could be tested in dried format[32-35], temperature control systems such as phase-change materials could be implemented[30, 31] and also electromagnet could be used instead of magnet, therefore an automated closed system (reducing contamination) with improved dynamic range could be achieved.

Methods

LAMP Assay:

The assay used in this study is similar to the assay reported in the work of Kong et al.[22] using the HNB and Evagreen dye combination in a loop-mediated isothermal DNA amplification. Unless otherwise stated, all components of the assay reaction mixture were purchased from Sigma, and all primers were purchased from Invitrogen. LAMP reaction mix consists of 20 mM Tris-HCl (pH 8.8), 10 mM KCl, 10 mM ammonium sulfate, 8 mM magnesium sulfate, 1 M betaine, 0.1% Triton-X 100, 120 μM HNB, 1.25 μM Evagreen (Biotium), 1.6 mM dNTPS (Invitrogen), 0.64 μM FIP and BIP, 0.08 μM F3 and B3, 0.16 μM Loop F and Loop B, 0.32 units/μL Bst DNA polymerase large fragment (New England Biolabs) in ultrapure DNase/RNase free water (Invitrogen). 100 μL volumes of reaction buffer were prepared for filling each of the reaction wells.

LAMP Primers:

FIP:CAGCCAGCCGCAGCACGTTCGCTCATAGGAGATATGGTAGAGCCGC

BIP:GAGAGAATTTGTACCACCTCCCACCGGGCACATAGCAGTCCTAGGGACAGT

F3:GGCTTGGCTCTGCTAACACGTT

B3:GGACGTTTGTAATGTCCGCTCC

LoopF:CTGCATACGACGTGTCT

LoopB:ACCATCTATGACTGTACGCC

Then λ DNA (Thermo Fisher) serially diluted in a solution of concentrated Ferumoxytol, were introduced at the inlet reservoir where different dosages of drops were delivered to 100 μl of reaction mix in wells.

Cell-Phone-Based Portable Fluorescent Reader: The mobile phone reader device was prepared by integrating a 3D printed opto-mechanical attachment with the camera module of a smartphone (Nokia Lumia 1020). All parts are designed by software Autodesk Inventor, and printed by Stratasys Dimension 3D printer. A 462nm 2W laser diode (DTR's Laser Shop) was used as the excitation light source and illuminated the sample at an approximately 75o incidence angle. An external lens (f=15 mm, Edmund Optics) together with the mobile phone camera lens form a two-lens imaging system providing a field of view of approximately 10mm diameter. An emission filter (BP 525/25 nm, Edmund Optics) was placed in between the mobile phone camera lens and external lens to separate fluorescent signals from the excitation backgrounds. To adjust focus, both sample holder and laser diode were mounted on a mini precision translational stage (DT 12, Thorlabs). The estimated cost of the mobile phone attachment is around 200 USD not including the optical filter.

Magnetic nanoparticles: The magnetic nanoparticle used here is concentrated Ferumoxytol (AMAG pharmaceuticals), which is a FDA approved drug used for treatment of iron deficiency,

and contains 20 nm sugar coated magnetic nanoparticles, which are ideal for avoiding interference with assay performance. The nanoparticles are small enough so that they will not sediment. Ferumoxytol is concentrated enough for a fast drop formation process, therefore we have centrifuged the original solution for 2 hours and 14000 rpm and then removed top 30 percent of solution and used the bottom concentrated fraction for mixing with the DNA sample to be used in the process.

Oils and surface coatings: Pico-surf (Dolomite) and Fluorosurfactant in FC 40 (RAN biosciences) have been tested as oils. Fluoro-surfactant in FC 40 has less auto-fluorescence and the results presented in figure5 are imaged with this oil. For FC 40 before injecting oil, device should be filled with 2 percent (trichloroIJ1H,1H,2H,2H- perfluorooctyl) silane (Sigma Aldrich) in FC 40 for 30 minutes, and for pico-surf, Rain-x should be used for 30 minutes to make the surfaces fluorinated.

Device: The size of the sample reservoir and the wells can be adjusted using the size of the punch that is used during the device fabrication. The device is made of PDMS bonded to a glass slide and the mold is fabricated using soft lithography method[2].

Magnet: In this controlled release platform, a small magnet (K&J magnetics-D68) is used for generating droplets containing sample mixed with magnetic nanoparticles until the desired dosage volume of the sample is emulsified from the reservoir.

ACKNOWLEDGMENT

The work is funded by NSF grant No. 1332275.

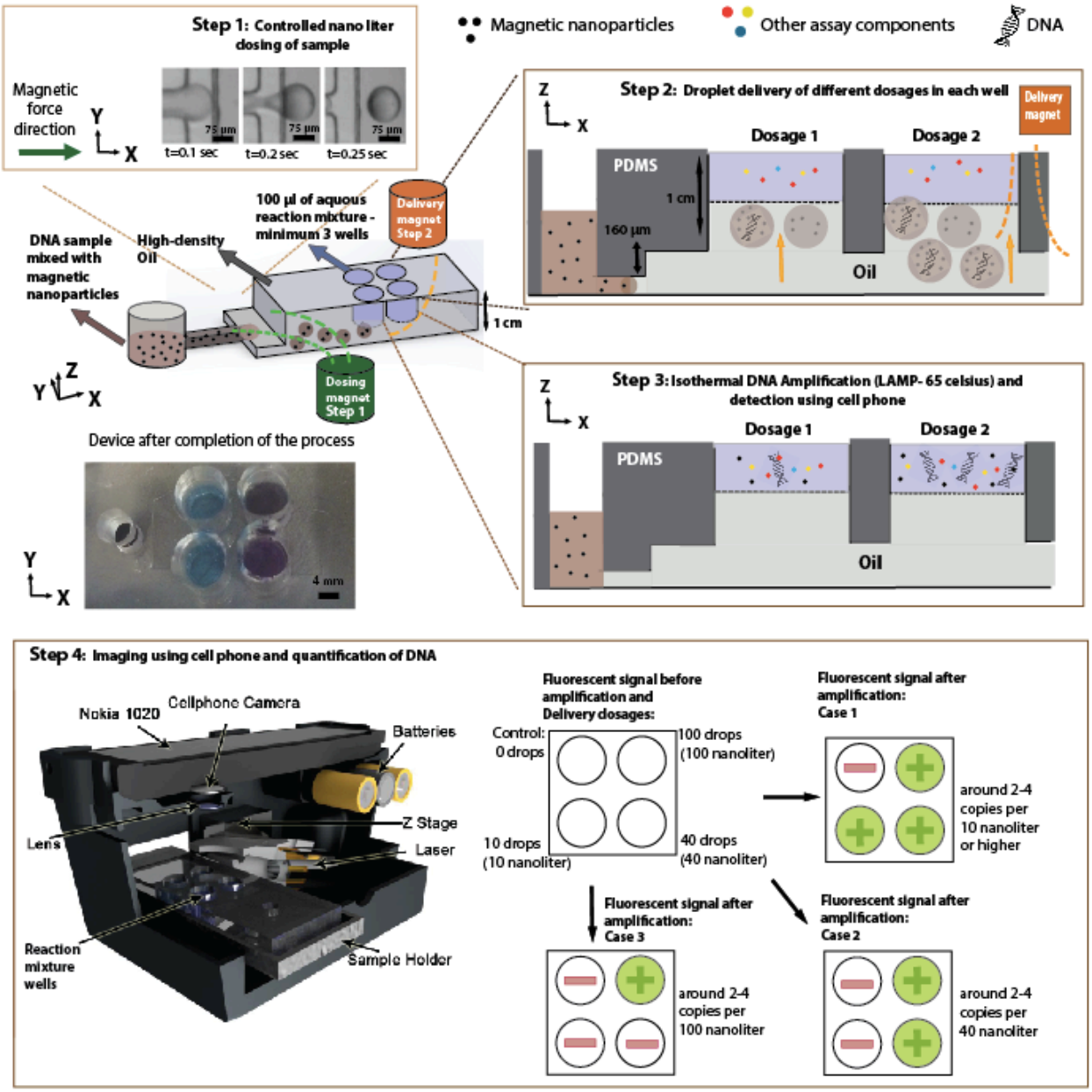

Figure 1: Operation steps of magnetic nano dispensing for quantification of DNA: The step emulsification device with one connecting channel from inlet reservoir to continuous-phase reservoir is used for precise nanoliter dosing and delivery using an external magnet. Continuous-phase region is filled with oil and inlet reservoir is filled with magnetic nanoparticles mixed with DNA sample. Step 1) Magnetic field is applied and fluid is attracted toward the magnet and

droplets are generated after the fluid passes the step. Number of generated droplets depends on the actuation time using magnet. Step 2) Then magnet is placed on top of one of the reaction wells containing reagents and the generated droplets in previous step are delivered to the well and merged with the assay components. This process continues until different desired nanoliter dosages of sample are delivered to designated wells. Step 3) the amplification process starts at 65 degrees Celsius. Step 4) based on the number of bright wells imaged with cell-phone after 75 minutes, the concentration of the lambda DNA in the original sample is determined. Number of wells and the delivered sample dosages could be easily adjusted and increased for multiplexing for different reactions for quantification of different biomolecules.

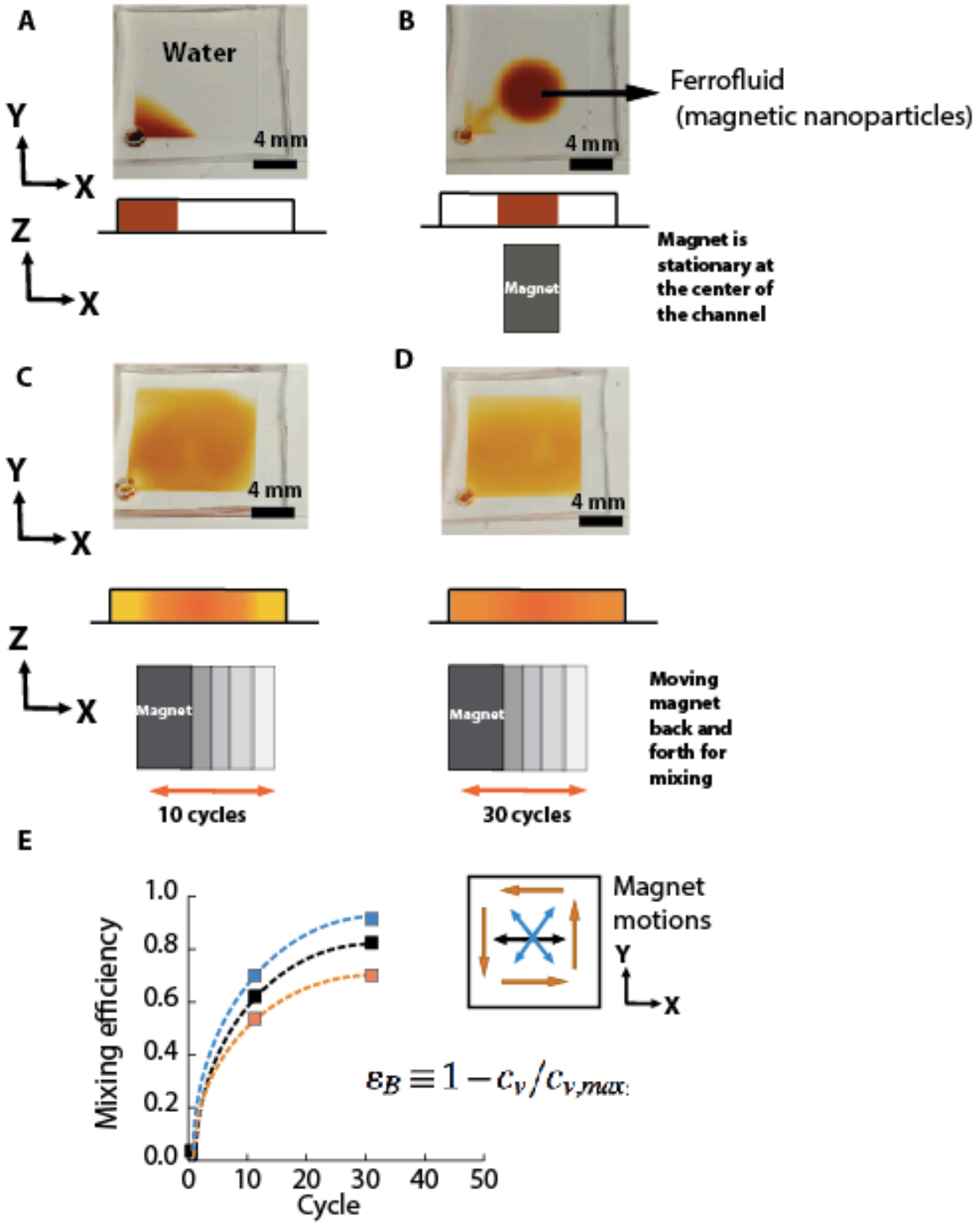

Figure 2: Magnetic mixing process: A) the square channel, which is a bit larger than the inlet reservoir in the amplification experiments for better visualization of the process, is filled with

water and the magnetic nanoparticle solution is then introduced at the inlet. Without presence of the magnetic field, only slow diffusion will contribute to mixing which is negligible. B) By locating the magnet below the center of the channel, magnetic solution will be attracted toward the center. C, D) By starting to move the magnet back and forth (cycles) along the channel, the magnetic solution and the water start to mix and a uniform intensity starts to appear across the channel. E) Mixing efficiency ($\mathbf{1 - cv/cv_{max}}$) for different type of motions of magnet is shown and mixing efficiency around 85 percent is achieved in about 1 minute.

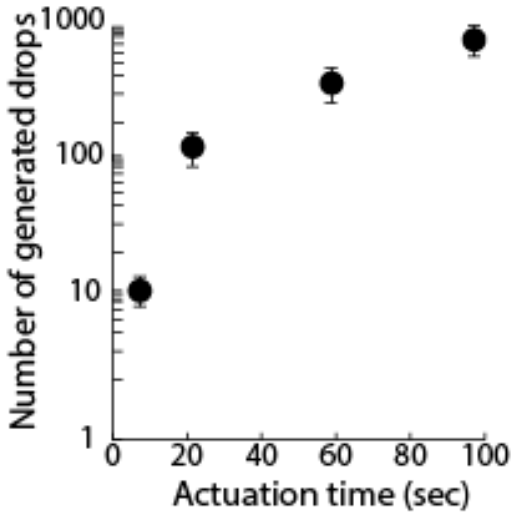

Figure 3: Dosing process: Number of generated nanoliter droplets for different interval of applying magnetic field using the magnet is shown. The standard deviation is less than 10 percent (10 percent of total volume of generated droplets for each case).

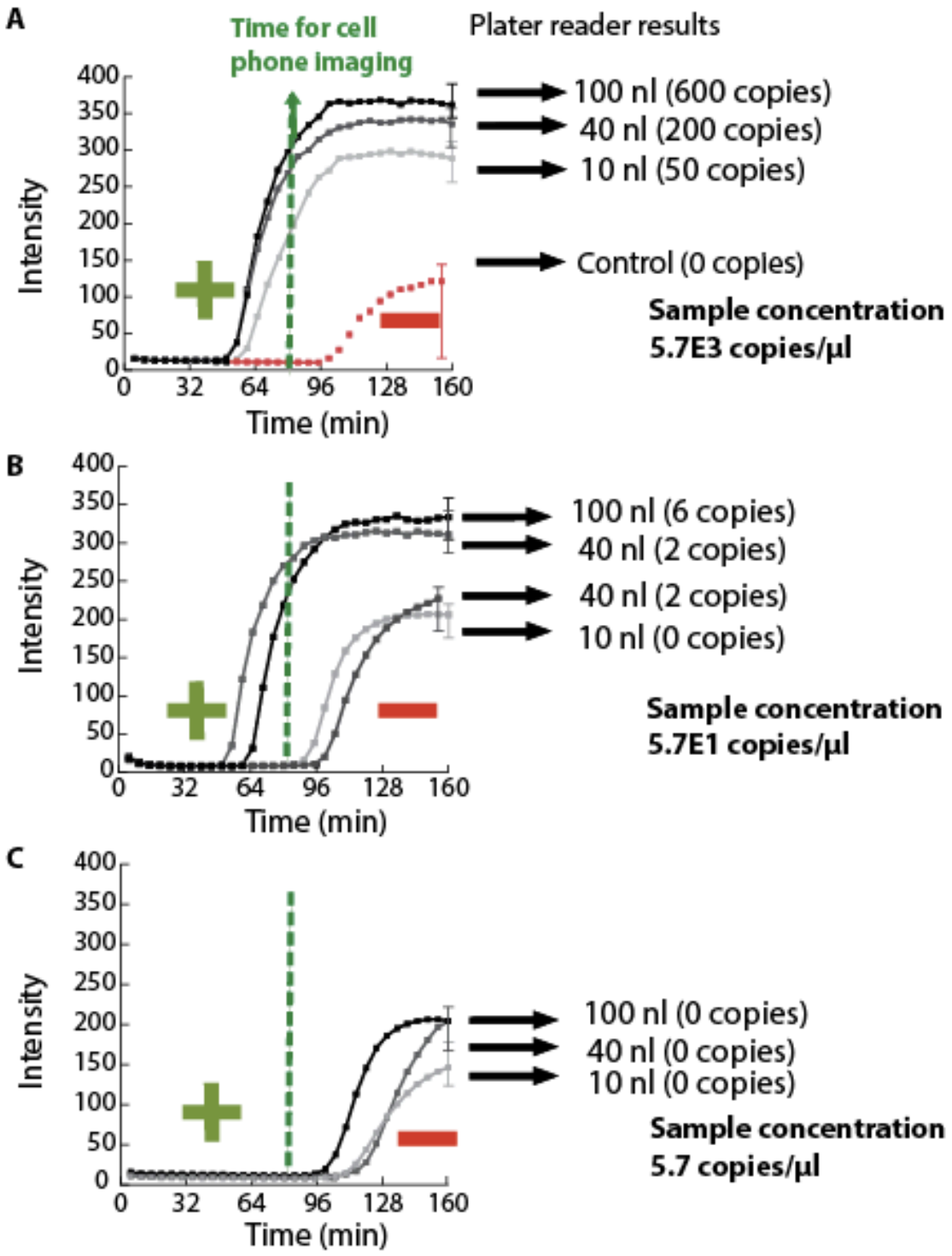

Figure 4: Plate reader testing for determining the best time for end-point measurement using cell phone. Results for 3 different DNA concentrations in the original sample are presented. For each

case, 10 drop (nl), 40 drop (40 nl), and 100 drop (100 nl) cases are tested. Control case is shown in the first graph. Numbers of copies are estimated based on the original DNA concentration and the total volume of generated droplets for each dosage. For the graph (A) all of the dosages result amplified signal after 60 minutes because of high concentration of DNA. However in graph (B) for 40 nl case (estimated around 2 copies) sometimes it results amplified signal and sometimes it does not. That could either be due to the fact that we might not have any DNA in that dosage of droplets or there is DNA but it does not get amplified due to extremely low number. For graph (C) none of the dosages are amplified due to low concentration of DNA as expected. Considering all graphs, 75 minutes is a good time point for performing the end-point imaging using cell phone for quantification of DNA due to a goof signal ratio compared to control and also avoiding false positive cases. Error bars (showing minimum and maximum) are shown only for the last data points to keep visibility of the data points. The error bar calculated based on three different experiments done for each case (showing minimum and maximum) is less than 15 percent for all data points (shown only for last data points to keep visibility of the other data points).

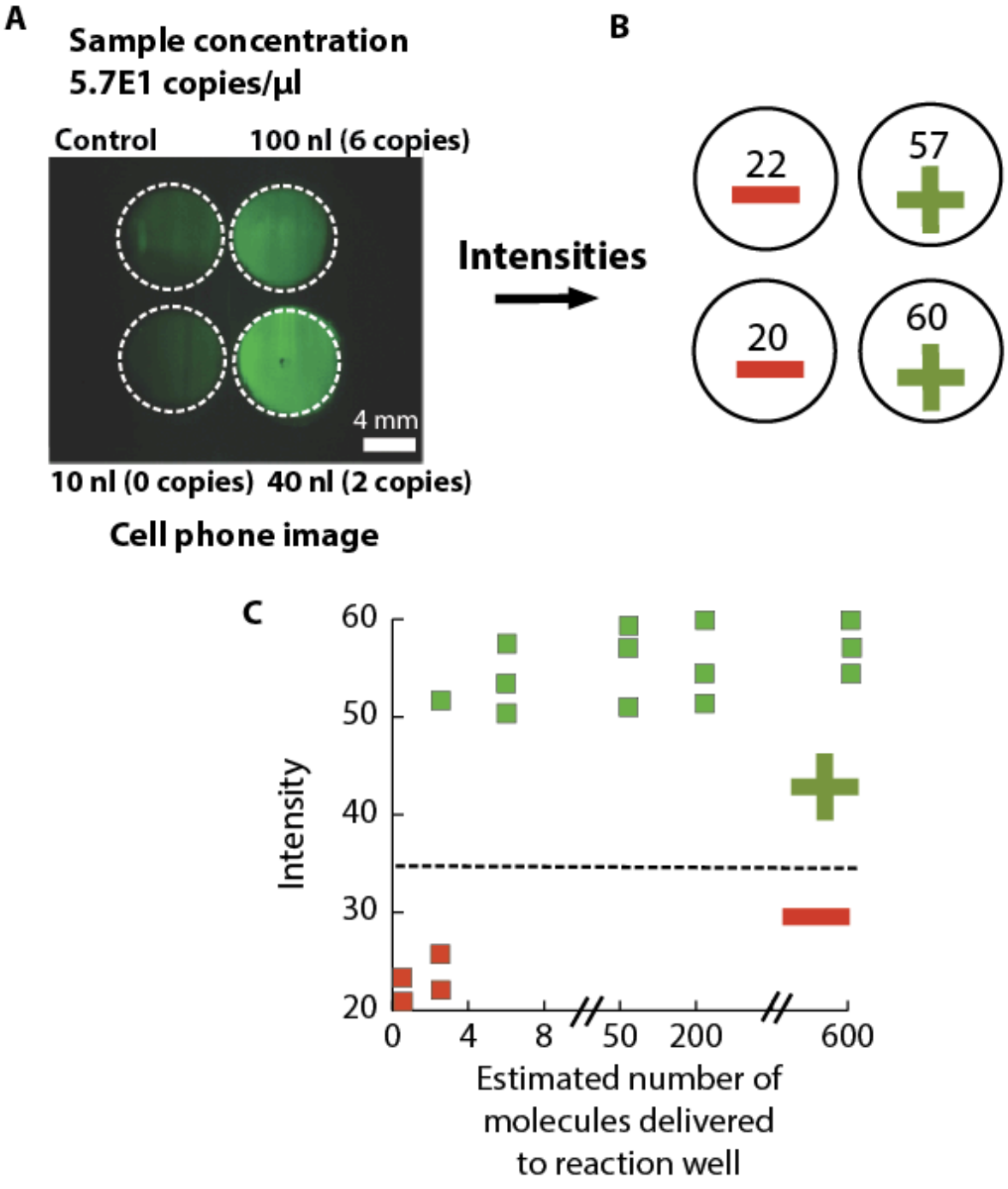

Figure 5: Cell phone results: Fluorescent images taken by cell phone after 75 minutes heating at 65 Celsius for concentrations A) 5.7E1 copies/µl. B) Corresponding intensities of each well (averaged over 50 pixels around the center of each well). C) Summary of all the experiments

done using cell phone imaging after 75 minutes for different dosages of droplets delivered. Instead of dosages, estimated number of copies delivered based on the total volume of drops delivered, is reported in the graph. As it is shown, for amplified signal, intensity is around 60 and for control it is around 20.

SUPPLEMENTARY: INTEGRATING A POROUS MEMBRANE IN A DROPLET MICROFLUIDIC DEVICE

Either for 1) the magnetic droplet dosing previous device presented when the oil has lower density than reaction mixture or

2) for implantable/wearable controlled drug delivery using ferrofluids

(Drugs mixed with or made with magnetic nanoparticles)

Here we used Nylon membrane:

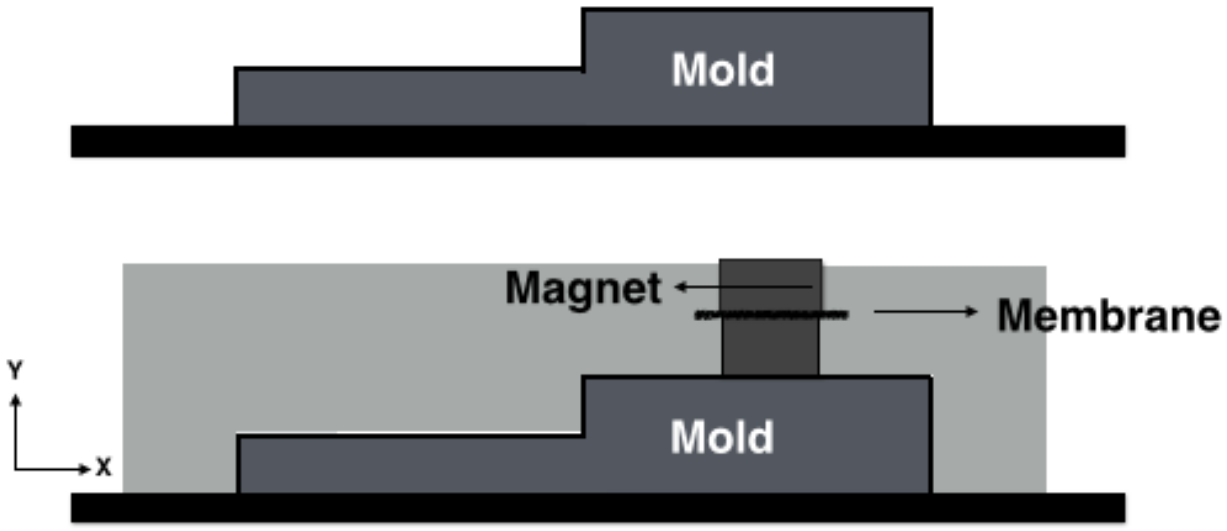

Supplementary figure1: Step 1) Mold structure and the membrane that is pinched between two magnet to avoid wetting after the PDMS is poured. After PDMS is curd magnets could be removed and porous membrane is integrated in the device (next figure)

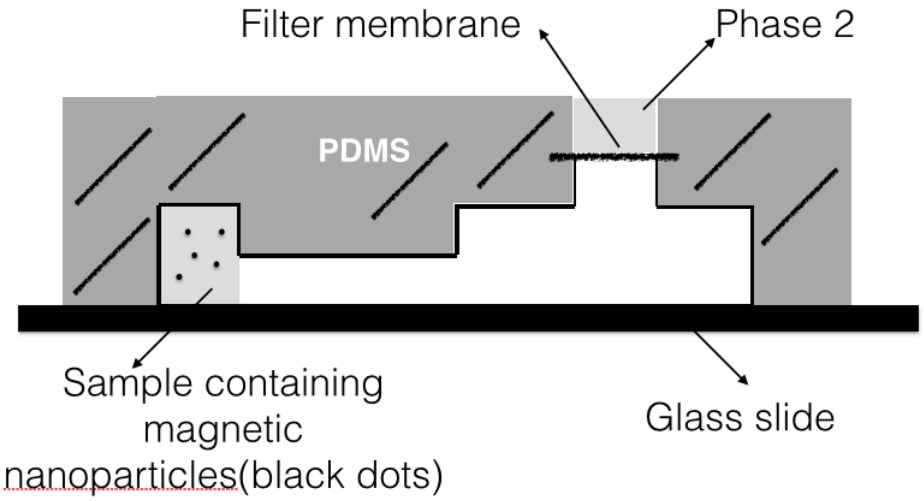

Supplementary figure2: Step 2) Device is bonded to a glass slide. Another layer is also bonded or clamped on top to enclose the fluid.

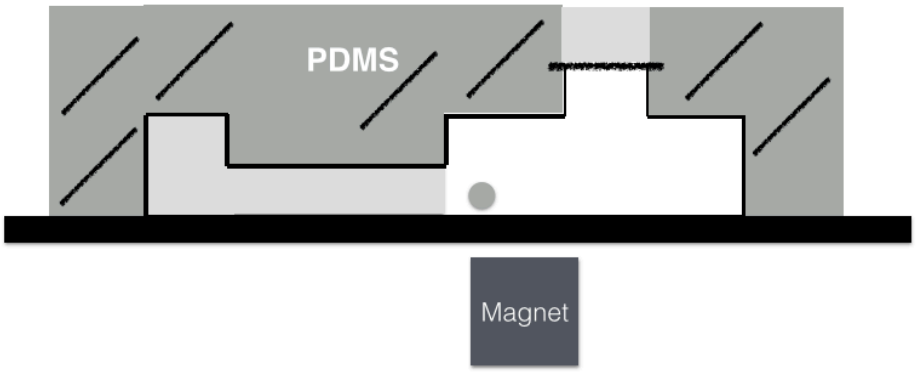

Supplementary figure 3: Step 3) By applying external magnetic field using a magnet or a varying magnetic field droplets are controllably generated.

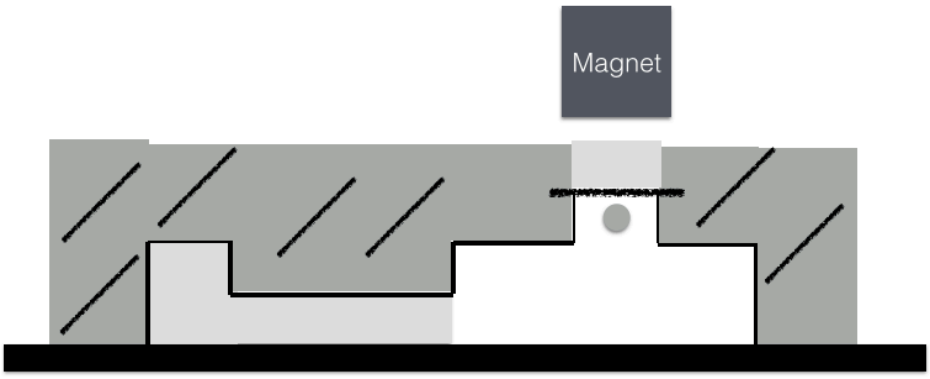

Supplementary figure 4: Step 4) By changing the direction of the magnetic force, droplets are attracted toward the filter membrane.

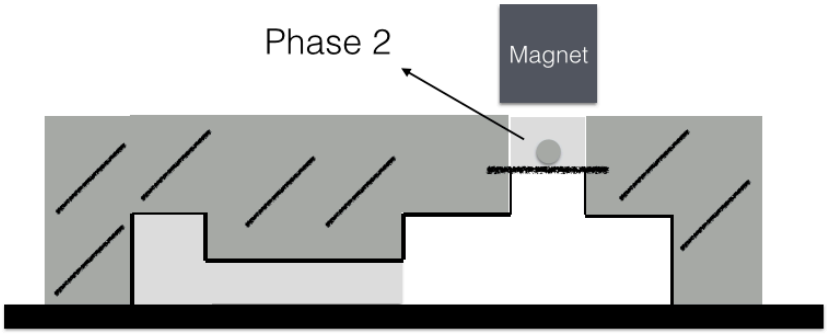

Supplementary figure 5: Step 5) By keeping the magnetic force at the same location droplets start to squeeze through the membrane and enter the second phase.

REFERENCES

(1) Sista, R.; Hua, Z.; Thwar, P.; Sudarsan, A.; Srinivasan, V.; Eckhardt, A.; Pollack, M.; Pamula, V. Development of a digital microfluidic platform for point of care testing 2008. Lab on a Chip, 8, 2091-2104.

(2) Kahkeshani, S.; Di Carlo, D. Drop formation using ferrofluids driven magnetically in a step emulsification device. Lab on a Chip 2016, 16, 2474-2480.

(3) Srinivasan, V.; Pamula, V.K.; Fair, R.B. An integrated digital microfluidic lab-on-a-chip for clinical diagnostics on human physiological fluids. Lab on a Chip 2004, 4, 310-315.

(4) Yager, P.; Edwards, T.; Fu, E.; Helton, K.; Nelson, K.; Tam, M. R.; Weigl, B. H. Microfluidic Diagnostic Technologies for Global Public Health. Nature 2006, 442, 412−418.

(5) Niemz, A.; Ferguson, T. M.; Boyle, D. S. Point-of-Care Nucleic Acid Testing for Infectious Diseases. Trends Biotechnol. 2011, 29, 240− 250.

(6) Rodriguez-Manzano, J.; Karymov, M.A.; Begolo, S.; Selck, D.A.; Zhukov, D.V.; Jue, E.; Ismagilov, R.F. Reading out single-molecule digital RNA and DNA isothermal amplification in nanoliter volumes with unmodified camera phones. ACS nano 2016, 10, 3102-3113.

(7) Dineva, M. A.; Mahilum-Tapay, L.; Lee, H. Sample Preparation: A Challenge in the Development of Point-of-Care Nucleic Acid-Based Assays for Resource-Limited Settings. Analyst 2007, 132, 1193.

(8) Berg, B.; Cortazar, B.; Tseng, D.; Ozkan, H.; Feng, S.; Wei, Q.; Chan, R. Y. L.; Burbano, J.; Farooqui, Q.; Lewinski, M.; Di Carlo, D.; Garner, O. B.; Ozcan, A. Cellphone-Based

Hand-Held Microplate Reader for Point-of-Care Testing of Enzyme-Linked Immunosorbent Assays. ACS Nano 2015, 9, 7857−7866.

(9) Laksanasopin, T.; Guo, T. W.; Nayak, S.; Sridhara, A. A.; Xie, S.; Olowookere, O. O.; Cadinu, P.; Meng, F.; Chee, N. H.; Kim, J.; Chin, C. D.; Munyazesa, E.; Mugwaneza, P.; Rai, A. J.; Mugisha, V.; Castro, A. R.; Steinmiller, D.; Linder, V.; Justman, J. E.; Nsanzimana, S.; et al. A Smartphone Dongle for Diagnosis of Infectious Diseases at the Point of Care. Sci. Transl. Med. 2015, 7, 273re1.

(10) Ozcan, A. Mobile Phones Democratize and Cultivate next- Generation Imaging, Diagnostics and Measurement Tools. Lab Chip 2014, 14, 3187−3194.

(11) Besant, J. D.; Das, J.; Burgess, I. B.; Liu, W.; Sargent, E. H.; Kelley, S. O. Ultrasensitive Visual Read-out of Nucleic Acids Using Electrocatalytic Fluid Displacement. Nat. Commun. 2015, 6, 6978.

(12) Tanner, N. A.; Zhang, Y.; Evans, T. C., Jr. Visual Detection of Isothermal Nucleic Acid Amplification Using pH-Sensitive Dyes. BioTechniques 2015, 58, 59−68.

(13) Chou, H. P.; Spence, C.; Scherer, A.; Quake, S. A Microfabricated Device for Sizing and Sorting DNA Molecules. Proc. Natl. Acad. Sci. U. S. A. 1999, 96, 11−13.

(14) Chin, C.D.; Linder, V.; Sia, S.K. Commercialization of microfluidic point-of-care diagnostic devices. Lab on a Chip 2012, 12, 2118-2134.

(15) Du, W.; Li, L.; Nichols, K.P.; Ismagilov, R.F. SlipChip. Lab on a Chip 2009, 9, 2286-2292.

(16) Shen, F.; Sun, B.; Kreutz, J.E.; Davydova, E.K.; Du, W.; Reddy, P.L.; Joseph, L.J.; Ismagilov, R.F. Multiplexed quantification of nucleic acids with large dynamic range using multivolume digital RT-PCR on a rotational SlipChip tested with HIV and

hepatitis C viral load. Journal of the American Chemical Society 2011, 133, 17705-17712.

(17) Craw, P.; Balachandran, W. Isothermal nucleic acid amplification technologies for point-of-care diagnostics: a critical review. Lab on a Chip 2012, 12, 2469-2486.

(18) Asiello, P.J.; Baeumner, A.J. Miniaturized isothermal nucleic acid amplification, a review. Lab on a Chip 2011, 11, 1420-1430.

(19) Notomi, T.; Okayama, H. Loop-Mediated Isothermal Amplification of DNA. Nucleic Acids Res. 2000, 28, e63.

(20) Nagamine, K.; Hase, T.; Notomi, T. Accelerated Reaction by Loop-Mediated Isothermal Amplification Using Loop Primers. Mol. Cell. Probes 2002, 16, 223−229.

(21) Goto, M.; Honda, E.; Ogura, A.; Nomoto, A.; Hanaki, K. I. Colorimetric Detection of Loop-Mediated Isothermal Amplification Reaction by Using Hydroxy Naphthol Blue. BioTechniques 2009, 46, 167.

(22) Kong, J.E.; Wei, Q.; Tseng, D.; Zhang, J.; Pan, E.; Lewinski, M.; Garner, O.B.; Ozcan, A.; Di Carlo, D. Highly Stable and Sensitive Nucleic Acid Amplification and Cell-Phone-Based Readout. ACS nano 2017.

(23) Selck, D. A.; Karymov, M. A.; Sun, B.; Ismagilov, R. F. Increased Robustness of Single-Molecule Counting with Microfluidics, Digital Isothermal Amplification, and a Mobile Phone versus Real-Time Kinetic Measurements. Anal. Chem. 2013, 85, 11129−11136.

(24) Ahmad, F.; Hashsham, S. A. Miniaturized Nucleic Acid Amplification Systems for Rapid and Point-of-Care Diagnostics: A Review. Anal. Chim. Acta 2012, 733, 1−15.

(25) Zhu, Q. Y.; Gao, Y. B.; Yu, B. W.; Ren, H.; Qiu, L.; Han, S. H.; Jin, W.; Jin, Q. H.; Mu, Y. Self-Priming Compartmentalization Digital LAMP for Point-of-Care. Lab Chip 2012, 12, 4755−4763.

(26) Rane, T.D.; Chen, L.; Zec, H.C.; Wang, T.H. Microfluidic continuous flow digital loop-mediated isothermal amplification (LAMP). Lab on a Chip 2015, 15, 776-782.

(27) Gansen, A.; Herrick, A. M.; Dimov, I. K.; Lee, L. P.; Chiu, D. T. Digital LAMP in a Sample Self-Digitization (Sd) Chip. Lab Chip 2012, 12, 2247−2254.

(28) Ober, T.J.; Foresti, D.; Lewis, J.A. Active mixing of complex fluids at the microscale. Proceedings of the National Academy of Sciences 2015, 112, 12293-12298.

(29) Nazockdast, E.; Morris, J.F. Pair-particle dynamics and microstructure in sheared colloidal suspensions: Simulation and Smoluchowski theory. Physics of Fluids 2013, 25, 420-452.

(30) Cordray, M. S.; Richards-Kortum, R. R. Review: Emerging Nucleic Acid-Based Tests for Point-of-Care Detection of Malaria. Am. J. Trop. Med. Hyg. 2012, 87, 223−230.

(31) Liao, S. C.; Peng, J.; Mauk, M. G.; Awasthi, S.; Song, J.; Friedman, H.; Bau, H. H.; Liu, C. Smart Cup: A Minimally-Instrumented, Smartphone-Based Point-of-Care Molecular Diagnostic Device. Sens. Actuators, B 2016, 229, 232−238.

(32) Lafleur, L.; Bishop, J. D.; Heiniger, E. K.; Gallagher, R. P.; Wheeler, M. D.; Kauffman, P. C.; Zhang, X.; Kline, E.; Buser, J.; Kumar, S.; Byrnes, S. A.; Vermeulen, N. M. J; Scarr, N. K.; Belousov,Y.; Mahoney, W.; Toley, B. J.; Ladd, P. D.; Lutz, B. R.; Yager, P. A Rapid, Instrument-Free, Sample-to-Result Nucleic Acid Amplification Test. Lab Chip 2016, 16, 3777.

(33) Das, A.; Spackman, E.; Senne, D.; Pedersen, J.; Suarez, D. L. Development of an Internal Positive Control for Rapid Diagnosis of Avian Influenza Virus Infections by Real-Time Reverse Transcription-PCR with Lyophilized Reagents. J. Clin. Microbiol. 2006, 44, 3065−3073.

(34) Siegmund, V.; Adjei, O.; Racz, P.; Berberich, C.; Klutse, E.; Van Vloten, F.; Kruppa, T.; Fleischer, B.; Bretzel, G. Dry-Reagent-Based PCR as a Novel Tool for Laboratory Confirmation of Clinically Diagnosed Mycobacterium Ulcerans-Associated Disease in Areas in the Tropics Where M. Ulcerans Is Endemic. J. Clin. Microbiol. 2005, 43, 271−276.

(35) Glynou, K.; Kastanis, P.; Boukouvala, S.; Tsaoussis, V.; Ioannou, P. C.; Christopoulos, T. K.; Traeger-Synodinos, J.; Kanavakis, E. High-Throughput Microtiter Well-Based Chemiluminometric Genotyping of 15 H88 Gene Mutations in a Dry-Reagent Format. Clin. Chem. 2007, 53, 384−391.